10th SEMESTER

Surface Analysis of the Interface Between E-beam Evaporated Boron and Si(111)

May 31, 2024

Physics, Group FYS10
Department of Materials and Production, Aalborg University

AALBORG UNIVERSITET
STUDENTERRAPPORT

Department of Materials and Production
Physics
Skjernvej 4A
9220 Aalborg Øst

Title:
Surface Analysis of the Interface Between E-beam Evaporated Boron and Si(111)

Project:
10th semester

Project period:
1tst of February 2024 to
31st of May 2024

Project group:
Group FYS10

Participants:
Lukas B. Jensen
Jesper B. Laursen

E-mail:
lujens19@student.aau.dk
jlau19@student.aau.dk

Supervisor:
Kjeld Pedersen

Number of pages:
67

Finish date:
31st of May 2024

Abstract:

This project aims to investigate the interface of boron evaporated on the Si(111) surface, by means of XPS at the ASTRID2 synchrotron facility at the University of Aarhus. Before conducting XPS experiments we will investigate how to control the e-beam evaporator utilized in this project. This will be done at a LEED/Auger experimental setup at Aalborg University.

Relevant theory for LEED, AES, XPS, synchrotrons and semiconductors will be covered and the various experimental setups utilized in the project will be detailed.

For the XPS experiments we will investigate the surface states appearing in the valence band and the Si2p spectra. The dependence of the B1s transition on the boron thickness will be discussed and influence of carbon and oxygen contamination will be examined. Furthermore we will go over the positioning of the Fermi level and use this to determine the amount of doping in the Si(111) sample.

Preface

This report has been written in the period February 1st till May 31st. This project group is composed of 10th semester students at the Department of Materials and Production at Aalborg University and is supervised by Kjeld Pedersen. The content of this report is divided into Introduction, Theory, Experimental, Results and Discussion and Conclusion.

For citations the Vancouver reference system is utilized. If a single source was the main inspiration for the content of a section, it is cited in the beginning of the section. For sources used in stating specific information, the citation is made where it is relevant in the report.

All lineshapes stated in the report are obtained from CasaXPS. The values for IMFP used are from *Standard Reference Database 71* published by NIST[1].

We want to thank our supervisor Kjeld Pedersen, and research technician Peter Kjær for their guidence during the project. We also want to express our gratitude to beamline scientist Zheshen Li for supervising us during our beamtime at the ASTRID2 synchrotron.

Aalborg University, May 31, 2024

Contents

Symbols and Shorthands

AES	Auger Electron Spectroscopy
B	Boron
CPS	Counts Per Second
E_{exc}	Excitation Energy
$FWHM$	Full Width at Half Maximum
$IMFP$	Inelastic Mean Free Path
$LEED$	Low Energy Electron Diffraction
Si	Silicon
STM	Scanning Tunneling Microscope
T_g	Growth Temperature
UHV	Ultra-High Vacuum
XPS	X-ray Photoelectron Spectroscopy

Introduction 1

Throughout the 20th century, immense technological advancements in the field of material science made it possible to investigate the nature of different materials by means of imaging their surface, and studying their electronic structure. Theoretical breakthroughs such as electron diffraction[2] and the Auger effect[3], cleared the path for methods and techniques like low energy electron diffraction (LEED) and Auger electron spectroscopy (AES) and allowed for measurements with a much higher precision than previously possible. This is largely due to the development of ultra-high vacuum (UHV) equipment to minimize surface contaminants, ensuring a cleaner sample.

One of the biggest advancements in surface science techniques is the development of X-ray photelectron spectrospy (XPS). The first XPS spectrum was obtained by P.D. Innes in 1907[4]. The technique has gone through many evolutions throughout the last century, which has enabled the possibility for high resolution chemical analysis of different materials, by characterizing their surface structure. In modern times, the best XPS photon sources are synchrotrons, invented by Edwin McMillan[5].

Another notable advancement was the development of scanning tunnelling microscopy by Rohrer and Binning[6]. This surface imaging technique was revolutionary, as it allowed for high precision imaging of a material surface with atomic resolution. This technique produced the first high resolution image of the Si(111) surface, exhibiting the 7 × 7 reconstruction, by Binning *et al.*[7]. This lead to Takayanagi *et al.*[8], proposing the Dimer Adatom Stacking fault (DAS) model, which is widely regarded as the correct description of the Si(111) 7 × 7 surface.

The deeper understanding of different semiconductor surfaces, like silicon, that these surface techniques have provided, has revolutionized the electronics industry. For the manufacturing of electronic components, like transistor, the use of Si(100) is the industry standard. This preference comes from its high electron mobility and much more consistent high quality oxide layers, compared to Si(111) and Si(110). But the Si(111) surface might still be a suitable candidate for production of other components, like sensors or detectors.

For this project, the structure of the Si-B interface formed by boron deposition on a Si(111) substrate, will be investigated. This will be studied using XPS at the AU-MATline at the ASTRID2 facility of the University of Aarhus. In the 1990's, multiple articles studying the Si(111) $\sqrt{3} \times \sqrt{3}$-B reconstruction using XPS, decomposed the Si2p transition into three surface states and bulk, e.g. Grehk *et al.*[9] and Rowe *et al.*[10]. The issue was that there was no consensus on the origin of the surface states. But in 2021, Aldahhak *et al.*[11], decomposed the same reconstruction into 5 surface states and bulk, supported by DFT-calculations. We intend to verify these claims by measuring the Si2p transition using XPS. We have produced boron layers on Si(111) using e-beam evaporation. This has seemingly not been done before, as all the literature available produced the B-Si interface by means of annealing a highly boron doped Si(111) wafer. We will investigate whether this difference in methodology leads to new results. The use of evaporation enables us to investigate the interaction of Si-B at the interface at room temperature, which is not possible with the annealing method.

We also study the effect of oxygen and carbon contaminants, that are deposited on the Si(111) surface while depositing boron, on the Si2p and B1s transitions using XPS. This is of interest since these contaminants are difficult to eliminate, even after degassing the e-beam evaporator for several hours. Our experiments show that we are able to eliminate the oxygen residue, with sufficient degassing. However, carbon was present in all XPS scans made after deposition.

Information about the doping level the Si(111) samples used in this project was not available. We were however able to exploit the XPS measurements of the valence band to find the Fermi level position, which we could use to calibrate our measurements.

Theory 2

2.1 Auger Electron Spectroscopy

This section is based on *Solid Surfaces, Interfaces and Thin Films* by Hans Lüth[12].

Investigation of surface composition can be carried out by means of Auger electron spectroscopy (AES). In AES a core-level electron in the atom is removed by an electron gun, thus creating hole in the core energy levels. This allows an electron in a higher energy level to relax into the vacant state releasing energy in the process. The excess energy from this process can be transferred to another electron in the atom and if this energy is larger than the binding energy the electron is emitted and collected by a detector. The emitted Auger electrons thus have a predefined kinetic energy independent of the energy of the external electrons or photons which is given by

$$E_{kin} = E_{core} - E_{relax} - E_{Auger},$$

where E_{core}, E_{relax} and E_{Auger} are the binding energies of the core-level electron, the relaxed electron and the Auger electron with respect to the vacuum level. This process is called the Auger effect and is visualized i figure 2.1.

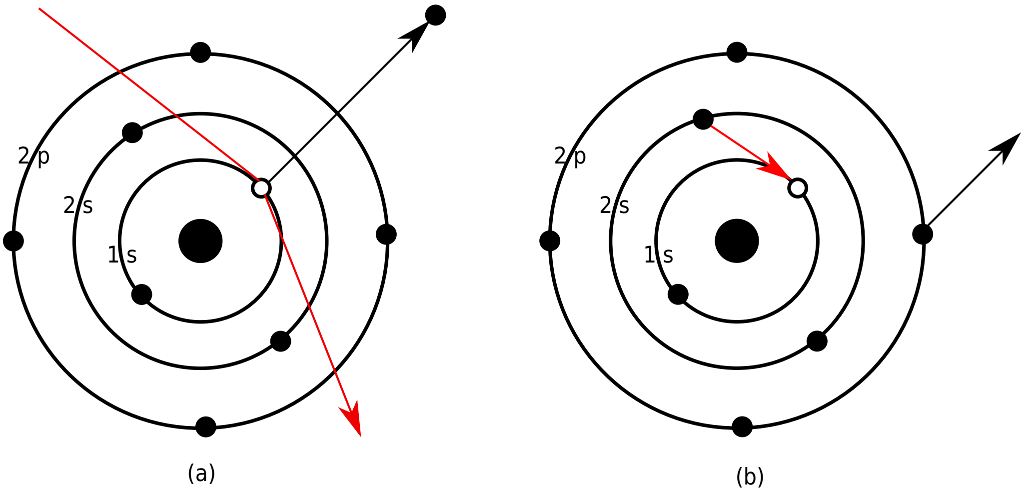

(a) (b)

Figure 2.1. (a) A core electron is removed by an external source. (b) A more energetic electron occupies the vacant core state and due to excess energy the atom emits an electron from a more energetic shell

The incident electron as well as the core electron leaves the atom with an energy that can not be predicted. Furthermore, the Auger process leaves the atom double-ionized. The Auger electron however takes on an energy defined by equation 2.1. This makes it possible to make chemical element analysis as is also done with XPS and also study the growth of thin films.

Spectroscopic nomenclature is used when referencing Auger transitions. If a hole is produced in the K shell an electron from the more energetic L_1 shell can fall into this vacancy. This in turn could transfer energy to an electron in the L_2 shell which has an ionization energy lower than the energy transferred. This Auger process is termed a KL_1L_2 process and is shown in the energy diagram in figure 2.2 along with a $L_1M_1M_1$ process.

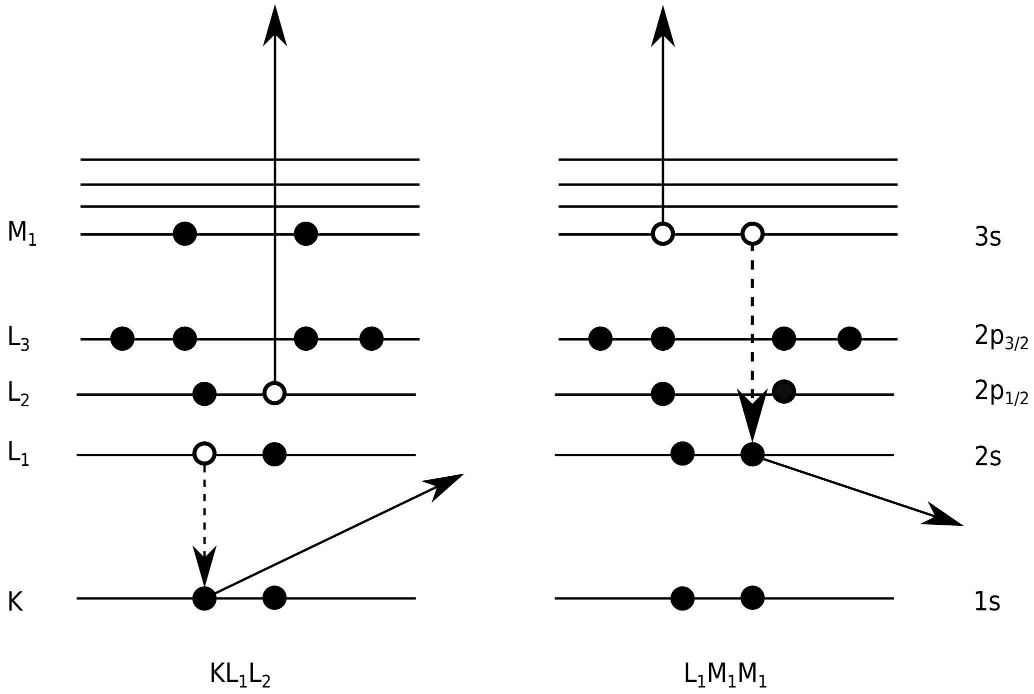

Figure 2.2. Energy diagram of the KL_1L_2 and $L_1M_1M_1$ Auger processes. The solid lines represent electrons emitted from the atom while dashed lines show interatomic transitions. After the KL_1L_2 process the atom is left with a hole in the L_1 shell and a hole in the L_2 shell. The $L_1M_1M_1$ process leaves the atom with two holes in the M_1 shell.

AES utilizes an electron gun that produces an electron beam with energy ranging from around 1000 eV up to 5000 eV. Due to low intensity of Auger signals, the AES spectrum is differentiated to more easily resolve the Auger peaks. In order to differentiate, a small alternating voltage $v = v_0 \sin \omega t$ is applied to the measured voltage, V. Hence the detector current can be expanded to the first order Taylor approximation

$$I(V + v_0 \sin \omega t) \simeq I_0 + \frac{dI}{dv} v_0 \sin \omega t.$$

This expression holds the sum of a constant and the current derivative times the applied modulation to the voltage. As a result of detecting the Auger spectra as a derivative, the characteristic Auger energies are referenced at the minimum of the derivative spectrum. This results in the actual maximum of the Auger peaks being shifted compared to the spectrum that has not been differentiated, as seen in figure 2.3.

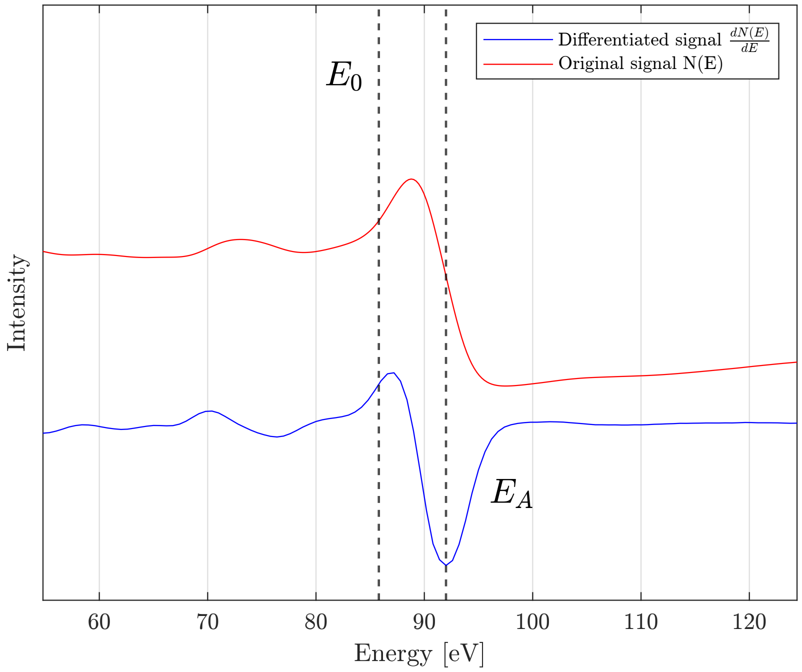

Figure 2.3. Spectrum of the Si2p signal obtained at an electron energy of 2 keV. Original Auger spectrum (red line) is compared to the differentiated Auger spectrum (blue line). The dashed line at energy E_0 indicates the position of the peak in the non-differentiated spectrum, whereas the dashed line at E_A indicates the minimum of the differentiated spectrum.

2.2 Low Energy Electron Diffraction

This section is based on *Surface Science: An Introduction* by Oura *et al.*[13], and *Solid Surfaces, Interfaces and Thin Films* by Lüth[14].

Low Energy Electron Diffraction or LEED is a surface science technique that is used to determine the surface structure of single-crystalline materials, by means of bombarding a surface sample with low energy electrons and observing the back-scattered electrons hitting a fluorescent screen.

2.2.1 Ewald Construction

In general, the energy range of electrons used when performing LEED is 30-200 eV. There are two main reasons why it is beneficial to choose low-energy electrons:

- The de Broglie wavelength of an electron is given by $\lambda = \frac{h}{\sqrt{2mE}}$. For the electrons in the LEED energy range, the de-Broglie wavelength is around 1-2 Å, so the wavelength of the electrons is in the order of the interatomic distances. This is crucial as for diffraction to occur, Bragg's Law must be satisfied, which requires the de broglie wavelength and interatomic distance to close in order of magnitude.
- Low-energy electrons have a very short mean free path, ensuring that elastic scattering mostly occurs in the topmost layers of the sample, making the technique particularly surface sensitive.

To understand the pattern observed with LEED, we introduce the Ewald sphere. If we assume that all scattering is elastic, and we have an electron with wave vector $\mathbf{k_i}$ incident on a sample, then the wave vector of the diffracted electron $\mathbf{k_d}$, must have the same length as the incident electron, due to conservation of energy. This means that we can create a sphere with radius $|\mathbf{k_i}|$, whose surface describes all the possible wave vectors of the scattered electron. This is called the Ewald sphere.

In the case of LEED, the assumption is that we are only diffracting electrons from the top-most layer of the sample, since we are using low-energy electrons. Thus the scattering problem becomes two-dimensional, as we are only dealing with the surface plane of the sample. This can essentially be described as the other atomic planes being infinitely far away from the surface, resulting in infinite periodicity in the direction normal to the surface, which in turn results in the reciprocal lattice points in the normal direction being infinitely densely packed, causing rods to form. This means that we can attribute each of these rods normal to the surface to a 2D surface lattice point, indexed by (h,k), as seen in figure. 2.4

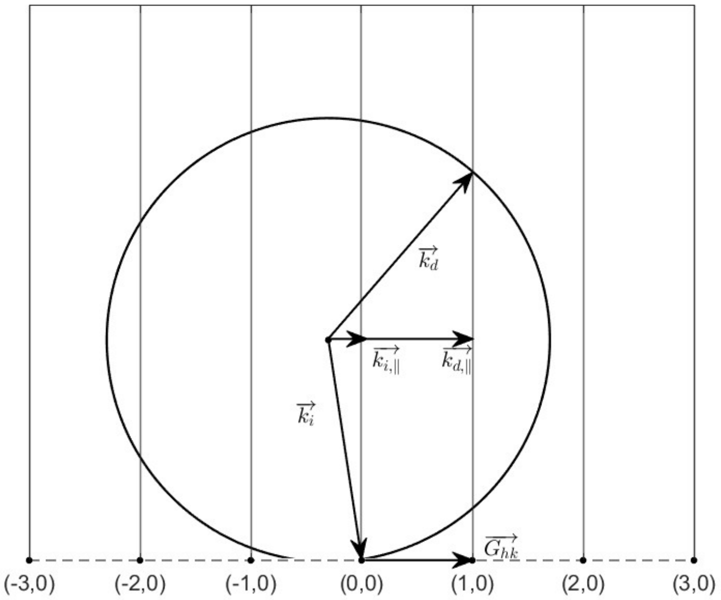

Figure 2.4. 2D Ewald sphere with incident electron $\vec{k_i}$ and diffracted electron $\vec{k_d}$, and their respective surface parallel components. Here the Bragg condition in equation 2.1, would be satisfied at reciprocal lattice points $\vec{G}_{10}$, $\vec{G}_{00}$, $\vec{G}_{-10}$ and $\vec{G}_{-20}$.

Since we have reduced our 3D problem to a 2D one, where periodicity in the direction normal to the surface is non-existent, the Bragg diffraction condition also reduces to one dependent only on the vector components parallel to the surface:

$$\mathbf{k_d^{\|}} - \mathbf{k_i^{\|}} = \mathbf{G_{hk}}, \tag{2.1}$$

where $\mathbf{k_d^{\|}}$, and $\mathbf{k_i^{\|}}$ are the diffracted and incident electron wave-vectors respectively, and $\mathbf{G_{hk}}$ is the 2D reciprocal lattice vector. The surface of the Ewald sphere, represents the elastic scattering of electrons, while each rod represents a reciprocal lattice vector $\mathbf{G_{hk}}$.

This means that the intersection between the Ewald sphere and a given rod, corresponds to points (hk) that fulfill the Bragg condition in equation 2.1. Diffraction will occur at these points, and the back-scattered electrons will appear as fluorescence on the LEED screen, revealing the surface structure of the sample. When constructing the Ewald sphere for 2D scattering, it is important than we start by having the incident wave vector terminate in $(hk) = (00)$. The origin of the incident wave vector will then be the center of the Ewald sphere, as seen in figure 2.4.

2.2.2 Interpreting LEED

In theory, LEED can be interpreted both qualitatively and quantitatively. By measuring the intensity of the diffracted beams as a function of the incident electron energy, accurate information about atomic positions can be attained. This however, is outside the scope of this project, so only the qualitative interpretation of LEED will be detailed in this section.

The first step of a qualitative analysis of a surface sample by LEED, is to determine the crystallographic quality of the surface. A uniform well-ordered surface of high quality will exhibit a LEED pattern with sharp well-defined spots, high contrast and low background noise. Any crystallographic imperfections or structural defects present on the sample surface, will cause the LEED spots to become broadened and less defined. If no LEED pattern at all is observed on a surface, it is an indication of the surface being amorphous. Additionally it can be an indication that the surface is not clean, and that material is deposited or adsorbed on the sample. Thus, if no LEED pattern is discernible it is advised to examine the sample with Auger spectroscopy to determine if contaminants are present.

After determining the quality of the surface, the spot geometry of the LEED pattern is examined to characterize the surface structure of the sample. If the LEED pattern of the crystal is already known, we can use this to determine the quality of the sample. The most simple structure we can observe in a LEED pattern is the 1x1 pattern. This occurs when the crystalline structure is bulk-like at the surface. This indicates that the periodicity of the crystal does not change as it terminates at the surface.

In many cases more complex structures form at the surface of the crystal, due to the atoms rearranging to minimize the free energy at the surface. This phenomena is called surface reconstruction. More generally we call a 2D surface like this that is different to the bulk a superstructure, which is characterized by their super-lattice. We now introduce the following notation for describing surface reconstructions. For a given superstructure, the superlattice can be thought of as a super unit-cell that can be defined from the lattice vectors of the bulk unit-cell

$$\mathbf{a_1^*} = p\mathbf{a_1} \tag{2.2}$$

$$\mathbf{a_2^*} = q\mathbf{a_2}. \tag{2.3}$$

p and q thus describe how much larger the superlattice is compared to the unit-lattice. We then denote the reconstruction for a specific cut (hkl) of a material M, as

$$M\{hkl\}(q \times p)R^{\circ}. \tag{2.4}$$

Where R° is the rotation of the superlattice vectors with respect to the bulk lattice vectors.

If a surface reconstruction occurs on a sample, the periodicity of the superlattice points will differ from the bulk lattice. This means the periodicity in reciprocal space will differ as well, leading to extra spots or superspots appearing in the LEED pattern. These extra spots correspond to the superlattice points in reciprocal space. Thus, we can get different LEED patterns for the same material, depending on the reconstruction that occurs, as seen in figure 2.5.

In addition to being able to distinguish between different reconstructions from the LEED pattern, the appearance of the superstructure points in the LEED pattern, is highly dependant on having a high quality clean surface. This means that checking to see if the reconstruction is visible in the LEED image is used to further determine the quality of the sample surface. E.g. for Si(111) the 1×1 pattern is more easily obtained than the 7×7 reconstruction which indicates a far cleaner surface.

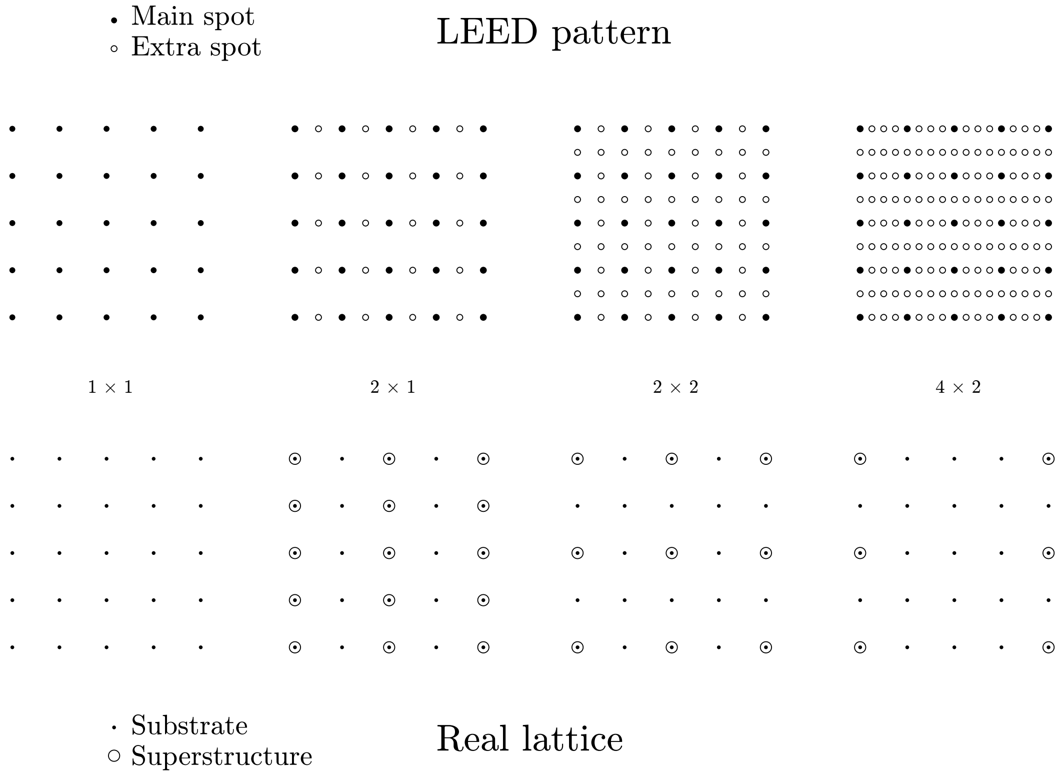

Figure 2.5. Real lattice and LEED pattern of crystal with different surface reconstructions. The unit-cell vectors of the real lattice are perpendicular and have the same length.

2.3 X-ray Photoelectron Spectroscopy

This section is based on *Solid Surfaces, Interfaces and Thin Films* by Lüth[14]

In surface science one of the most widely used experimental techniques to obtain information about occupied electronic states, is photoemission spectroscopy. The basis for photoemission spectroscopy is the photoelectric effect, which describes that electrons are emitted from a surface when irradiated by electromagnetic radiation. By irradiating a sample surface with photons, we can thus collect the emitted electrons and obtain information about the chemical composition of the sample, based on the kinetic energy of the electrons. When using X-ray photons, we call it X-ray Photoelectron Spectroscopy or XPS.

The rigorous approach to describing photoemission requires a complete quantum mechanical treatment of the full process. This approach treats the photoemission process from irradiating a surface, to an electron being emitted as a single step process. But this method is rather complicated, so instead we separate the complete process into three independent steps, to simplify the problem. These steps are as follows:

1. Excitation of an electron from an initial state, into a final state by irradiating the crystal with photons.
2. Propagation of an electron from the excited state to the surface.
3. Emission of the electron from the crystal surface to vacuum.

In reality, these steps are not independent from each other, which is why the one step process is more accurate than separating the process into three steps. But the three step model is sufficient for summarizing the overall photoemission process. For the first step, the excitation of an electron is described by Fermi's golden rule transition probability given as

$$W_{fi} = \frac{2\pi}{\hbar} |\langle f, \mathbf{k}| \mathcal{H} |i, \mathbf{k}\rangle|^2 \delta(E_f(\mathbf{k}) - E_i(\mathbf{k}) - \hbar\omega),$$

where $|\langle f, \mathbf{k}| \mathcal{H} |i, \mathbf{k}\rangle|$ describes the transition from the initial state i to the final state f, due to a perturbation $\mathcal{H}$ of the system occurring when a photon interacts with the crystal. E_i and E_f are the corresponding energies of these states and the delta-function is an energy conservation term as it only equals 1 when $E_f(\mathbf{k}) = E_i(\mathbf{k}) + \hbar\omega$.

The second step explains the propagation of an excited electron to the crystal surface. A large number of electrons are inelastically scattered in their journey to the surface, either by electron-plasmon or electron-phonon scattering, leading to energy loss. These electrons end up forming the natural background of a photoemission spectrum and are not of interest, since they can not provide information about state of the electrons initial energy E_i anymore. Instead, we are interested in electrons that make it to the surface without experiencing scattering. The probability of this occurring is dependent on the mean-free path, λ, of the excited electron. The mean-free path is a function of the energy E and wave vector, $\mathbf{k}$, of the electron. Thus the probability of transport to the surface, $D(E, \mathbf{k})$ is proportional to the mean-free path

$$D(E, \mathbf{k}) \propto \lambda(E, \mathbf{k}).$$

It is this dependence on the mean-free path that qualifies photoemmision as a surface technique. This is due to λ typically lying in the range of $5 - 20$ Å, which limits the depth of which we obtain useful information to layers close to surface.

The third step details the transmission of the excited electron from the surface into vacuum, i.e. emission of a photoelectron. Here we consider the scattering of a Bloch electron wave from the surface, and assume translational symmetry parallel, but not normal to the surface. Due to this symmetry, the transmission of an excited electron through the surface, must conserve the parallel component of the wave vector, leading to the equation

$$\mathbf{k}_{\parallel}^{ex} = \mathbf{k}_{\parallel} + \mathbf{G}_{\parallel},$$

where $\mathbf{k}_{\parallel}^{ex}$ is the electron wave vector outside the crystal, $\mathbf{k}_{\parallel}$ is the wave vector inside the crystal and $\mathbf{G}$ is the reciprocal lattice vector. We can construct the following energy conservation equation

$$E_{kin} = \frac{\hbar^2 k^{ex^2}}{2m} = \frac{\hbar^2}{2m}(k_{\parallel}^{ex^2} + k_{\perp}^{ex^2}) = E_f - E_{vac},$$

where E_{kin} is the energy of the electron outside the crystal, and E_{vac} is the energy of a free electron a rest in vacuum. From this equation we obtain the following expression

$$\hbar\omega = E_f - E_i = E_{kin} + \phi + E_b,$$

where E_b is the binding energy of the electron in relation to the Fermi level E_F. $\phi = E_{vac} - E_F$ is the work function and is given as the energy difference between the Fermi level and the vacuum level. The work function describes the minimum energy required to remove an electron from the crystal into vacuum. We can rewrite this equation to get

$$E_b = \hbar\omega - (E_{kin} + \phi).$$

This is an important equation for photoemission as it tells us how to translate the kinetic energy of an emitted photoelectron to the binding energy, depending on the photon energy used, and the specific work function. In surface techniques, like XPS, the energy of the photon source $h\nu$, is often referred to as the excitation energy, E_{exc}.

2.4 Synchrotron radiation

This section is based on Bulou *et al.*[15].

We will now describe the structure of a typical synchrotron, as well as the theoretical basis for the occurrence of synchrotron radiation.

A synchrotron consists of a large evacuated ring, called the storage ring. The storage ring facilitates the circulation of high-energy electrons at relativistic speeds. At specific points in the ring, the radiation emitted by the orbiting electrons is extracted into a tangential path by bending magnets and insertion devices, forming a so-called beamline. These beamlines connect to separate experimental setups, acting as their photon source.

The larger the storage ring is, the more beam-lines can be formed. This makes it possible to have multiple separate experimental setups running simultaneously, originating from the same synchrotron. Typically, the energy of the electrons in the storage ring is of the order of GeV, while the emitted photons are in the range of a few eV to hundreds of keV. As they radiate photons, the electrons in the storage ring are losing energy. This is replenished either by a radio-frequency chamber, or an auxiliary storage ring feeding the main ring electrons.

2.4.1 Brilliance

For synchrotrons, the measure of the spectral brightness, often called the brilliance, is the standard indicator of quality. The brilliance is defined as

$$\text{Brilliance} = \frac{\text{photons / second}}{(\text{mrad})^2(\text{mm}^2\text{ source area})(0.1\%\text{BW})}, \tag{2.5}$$

where $(\text{mrad})^2$ is the beam divergence, (mm^2 source area) is the source area and (0.1%BW) is 0.001 of the frequency range. As indicated by equation (2.5), to maximize the brilliance of a synchrotron source, we need to minimize the source area and beam divergence. The product of the source size and the beam divergence is called the emittance.

For synchrotrons, where specific narrow ranges of frequencies are used for experiments e.g. for XPS and UPS, the intensity per unit frequency is a better measure of the efficacy of a synchrotron, compared to using the flux.

2.4.2 Synchrotron Radiation

Synchrotron radiation is when an electron in a circular path emits light, caused by acceleration when the electrons changes direction in its travel. It is the case that all charged particles experiencing acceleration emit radiation. This phenomena will be explained here.

Electromagnetic waves are transverse waves, which means that the electric and magnetic fields oscillate in the direction perpendicular to propagation. In this case we only consider the electric field component of the EM radiation. The electric field lines of an isolated electron at rest emanate out radially from the particle. This means that for any observer, there will be no transverse component of the field, see figure 2.6. This in turn results in them observing no radiation.

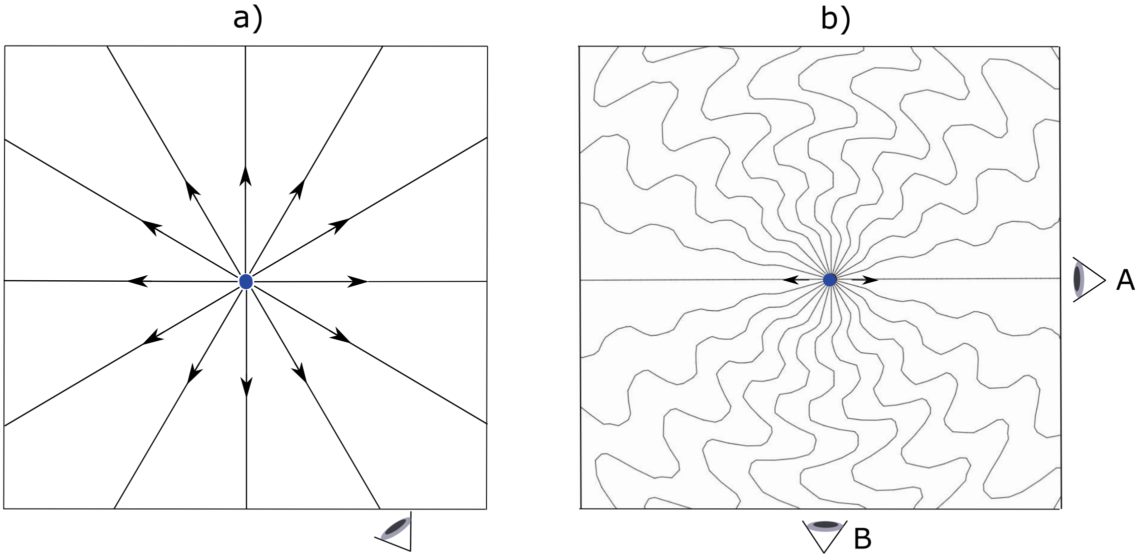

Figure 2.6. Electric field lines emanating from a free electron at *a*) rest, and *b*) when performing oscillatory motion. For an electron at rest, no transverse electric field component is apparent, no matter the position of the observer. For the oscillating electron, a transverse component is detected for any observer, except if situated on the axis of propagation, like observer *A*.

If instead the electron oscillates, the electric field lines will still emanate radially, but their origin will shift with the electron, inducing oscillatory motion in the field lines as well. As is illustrated in figure 2.6, an observer anywhere except along the axis of propagation, will register a transverse component of the electric field of the electron, meaning they will perceive light being emitted.

In the case of a synchrotron, the electrons experience acceleration due to a change in direction, caused by the bending magnets applying an external magnetic field. In addition, utilizing insertion devices like undulators and wigglers to oscillate the electrons, will produce radiation in the manner described in figure 2.6. The radiation emitted from the orbiting electrons have a large bandwidth, which makes it possible to select specific photon energies, by passing the radiation through a monochromator. For surface techniques like XPS, this is very useful as it enables measurements on different probing depths.

2.5 The Lambert-Beer Law

This section is based on *Optics* by Pedrotti[16].

When light travels through a material, in general some of the incident light will be scattered and absorbed by the material. In effect, not all light will be transmitted to the other side of the material. This situation is depicted in figure 2.7, where a light beam of intensity I_0 is incident on a slab of material and attenuated due to exchange of energy with the material.

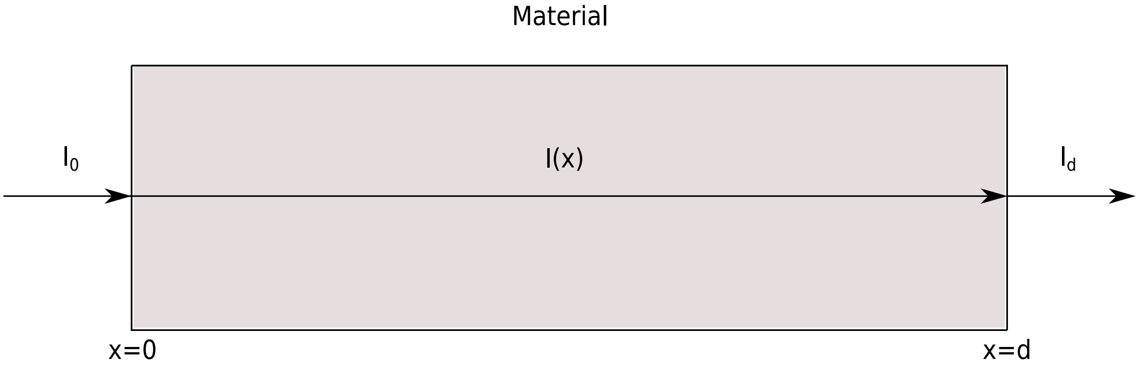

Figure 2.7. Light beam of intensity I_0 is incident on a slab of material. Inside the material the intensity is attenuated due to absorption and scattering. The intensity is a function of the materials attenuation coefficient and after travelling a distance $x = d$ in the material the intensity is equal to I_d.

Consider the situation in figure 2.7, where a beam of light travels in the positive x-direction, enters a material at $x = 0$, and exits at $x = d$. Now divide the material into infinitesimally thin segments of thickness dx. The intensity of the light that exits a segment is reduced compared to the light that enters the segment by

$$dI(x) = -\alpha I(x)dx,$$

where α is the attenuation coefficient. This yields a first order linear ordinary differential equation

$$\frac{dI(x)}{dx} = -\alpha I(x).$$

This equation has a simple solution on the form

$$I(x) = c \cdot \mathrm{e}^{-\alpha x}, \tag{2.6}$$

where c is a constant that we can determine from the initial condition $I(0) = I_0$. By inserting this into equation (2.6) we get that $c = I_0$, the intensity of the original beam. The Lambert-Beer law can now readily be written as

$$I(x) = I_0 \cdot \mathrm{e}^{-\alpha x}.$$

The depth of an atomic layer can be determined from this law if the attenuation coefficient is known.

2.6 Semiconductor Physics

This section is based on *Semiconductor Physics and Devices: Basic Principles* by Donald A. Neamen[17].

Basic solid state physics provides us with the theory of how electronic bands arise due to the periodic structure of a crystal[18] and from band theory the notions of valence band and conduction band arise.

Consider a silicon crystal, like the two-dimensional representation in figure 2.8. At zero kelvin, each silicon atom shares its four valence electrons with its four neighboring atoms, forming covalent bonds. In this way all silicon atoms in the crystal obtain eight electrons in their outer shell which is the most stable configuration. All valence electrons occupy states in the valence band which is filled. At the same time the conduction band is completely empty. In this situation no electrons are able move since all states in the valence band are occupied and the electrons do not posses the energy needed to jump into the conduction band.

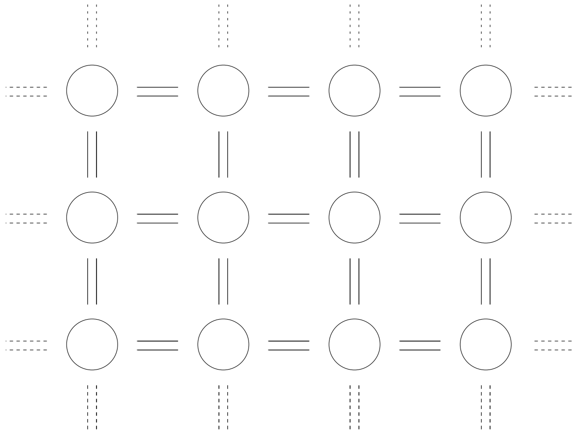

Figure 2.8. Two-dimensional sketch of a single crystal silicon lattice at zero kelvin. All silicon atoms share their 4 valence electrons with their four neighbors creating covalent bonds.

If we let the temperature increase above zero kelvin, thermal excitations result in electrons breaking the covalent bonds as can be seen in figure 2.9. As the electron takes off it leaves behind a “hole” which can be perceived as a positively charged empty state that can traverse the silicon crystal.

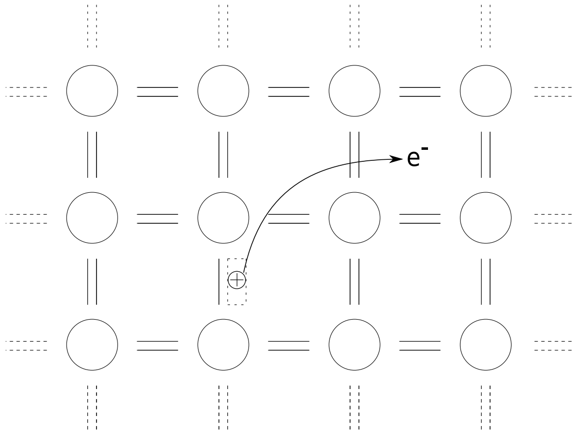

Figure 2.9. Two-dimensional sketch of a single crystal silicon lattice at temperature $T > 0K$. Thermal excitation has led the electron to break the covalent bonding and left its original state leaving behind a positively charged hole.

As the electron leaves its original state it jumps from the valence band into the conduction band. In the conduction band the electron can move to other unoccupied states and conduction can now take place. The same is possible the for the hole in the valence that can move to occupied states in the valence band. The situation is depicted in the energy-band diagram i figure 2.10, where also the band gap energy is shown as the difference between bottom of the conduction band, E_C and the top of the valence band, E_v.

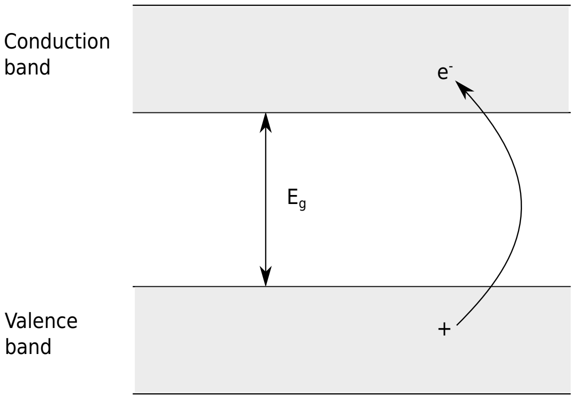

Figure 2.10. Energy-band diagram. When an electron is thermally excited from the valence into the conduction band it leaves behind a hole. Both can contribute to conduction since they can move to other states.

2.6.1 Density of States for Semiconductors

We will not derive the general form of the density of state per unit volume of a crystal in three dimensions, but merely state that it is given by

$$g(E) = \frac{4\pi(2m)^{3/2}}{h^3}\sqrt{E},$$

where m is the mass of a free electron bounded by a three dimensional infinite potential well. Extending this concept to semiconductors, the density of states in the conduction band and valence band can be found.

The general expressions for the density of states is derived by using the free electron model. Continuing using the model of a free electron in an infinite potential well we have that the energy is given by

$$E = \frac{p^2}{2m} = \frac{\hbar^2 k^2}{2m}.$$

This approximation holds well at the bottom of the conduction band, E_c, and at the top of the valence band, E_v, i.e. near $k = 0$. Hence we get

$$E = E_c + \frac{\hbar^2 k^2}{2m_n^*} \implies E - E_c = \frac{\hbar^2 k^2}{2m_n^*},$$

where m_n^* is the electron effective mass.

An electron near the bottom of the conduction band can be perceived as a free electron with the effective mass m_n^*. Thus density of states in the conduction band is given by

$$g_c(E) = \frac{4\pi(2m_n^*)^{3/2}}{h^3}\sqrt{E - E_c}, \tag{2.7}$$

and the density of states in the valence band is found in the same manner to be

$$g_v(E) = \frac{4\pi(2m_n^*)^{3/2}}{h^3}\sqrt{E_v - E}. \tag{2.8}$$

There are no allowed states in the band gap, hence $g(E) = 0$ for $E_v < E < E_c$. In the energy diagrams in figure 2.11 the density of states in the conduction and valence bands are indicated.

2.6.2 Fermi-Dirac Distribution

To determine the electron concentration in the conduction band, the hole concentration in the valence band we introduce the Fermi-Dirac probability distribution

$$f_F(E) = \frac{1}{1 + \exp\left(\frac{E-E_F}{kT}\right)}.$$

We will not argue for its validity but just assume that it gives the probability that a given state at energy E is occupied by an electron. E_F is the Fermi level, which defines the energy of the highest occupied state.

Since the Fermi-Dirac probability distribution gives the probability of a state being occupied and we know the density of states as found in equation (2.7) and (2.8), the electrons and holes respectively are distributed as

$$n(E) = g_c(E)f_F(E) \tag{2.9}$$

and

$$p(E) = g_v(E)[1 - f_f(E)]. \tag{2.10}$$

Hence the electron concentration per unit volume in the conduction band is found by integrating $n(E)$ over the whole conduction band. Similarly the hole concentration in the valence band is found by integrating $p(E)$ over the whole valence band. Figure 2.11 shows how the Fermi-Dirac probability function is related to the Fermi level and the distribution of electrons in the conduction band and holes in the valence band.

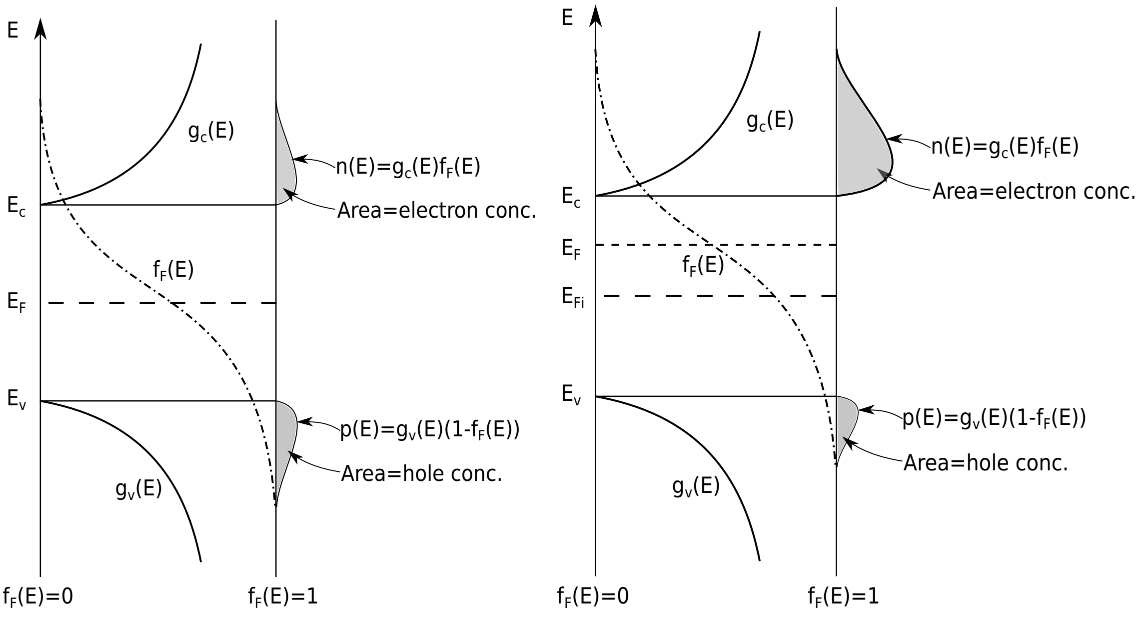

(a) *(b)*

Figure 2.11. Density of states functions in the conduction band and valence band, Fermi-Dirac probability distribution and E_c, E_F and E_v are indicated at the energy axis and $f_F(E)$ on the a x-axis for **(a)** an intrinsic semiconductor where $E_F = E_{Fi}$ and **(b)** an n-type semiconductor where the Fermi level is shifted towards the conduction band.

2.6.3 Electron Concentration

Electrons in the conduction band have energies $E > E_c$. If we assume that the Fermi level is within the band gap and $(E_c - E_F) \gg kT$ it follows that $(E - E_F) \gg kT$. In this limit the Fermi-Dirac distribution simplifies to the Boltzmann approximation

$$f_F(E) = \frac{1}{1 + \exp\left(\frac{E-E_F}{kT}\right)} \approx \exp\left(\frac{-(E-E_F)}{kT}\right).$$

By integrating equation (2.9) and applying the the Boltzmann distribution, we find the thermal equilibrium electron concentration

$$n_0 = n_i \exp\left[\frac{-(E_c - E_F)}{kT}\right], \tag{2.11}$$

where n_i is the intrinsic carrier concentration which is a material specific function of temperature. For silicon the intrinsic charge carrier concentration at room temperature is $n_i = 1.5 \cdot 10^{10}$ cm^{-3}.

Until now the notion of the intrinsic semiconductor has not been brought up. An intrinsic semiconductor is a pure semiconductor free of defects and with no impurity atoms. Hence n_i is the carrier concentration for such a semiconductor. The carrier concentration can be changed by doping the semiconductor. This means that some atoms are replaced by impurity atoms. Silicon is usually doped with either boron or phosphorus. In contrast the four valence electrons of silicon, phosphorus has five valence electron, i.e. an extra electron to contribute to the electron concentration. This adds negative electric charge and is called an n-type semiconductor. On the contrary boron has only three valence electrons meaning that the concentration of boron contributes to the hole concentration making a p-type semiconductor.

Since the carrier concentration is related to the Fermi-Dirac probability distribution by equations (2.9) and (2.10), the Fermi-Dirac probability distribution as depicted in figure 2.11 **(a)** shifts towards higher energies when the electron concentration increases as in the case of an n-type semiconductor, as seen in figure 2.11 **(b)**. As the Fermi level is decided by the distribution, it also shifts away from the intrinsic Fermi level towards higher energies. The opposite situation happens when a semiconductor is boron doped.

If a semiconductor only contains donor or acceptor impurity atoms the doping level can be calculated if the distance between the Fermi level and the intrinsic Fermi level is known. We will only state this result in equation (2.12). For a full derivation see Neamen[17].

$$n_0 = n_i \exp\left(\frac{E_F - E_{Fi}}{kT}\right) \tag{2.12}$$

One last result that we only state since its impact on our results is negligible, is the electron concentration for a compensated semiconductor where both donor and acceptor atoms are present

$$n_0 = \frac{(N_d - N_a)}{2}\sqrt{\left(\frac{(N_d - N_a)}{2}\right)^2 + n_i^2}. \tag{2.13}$$

Here N_d and N_a are concentrations of donor and acceptor impurity atoms, respectively. If only donor impurity atoms are present in the semiconductor and the electron concentration is known this simplifies to

$$N_d = \frac{n_0^2 - n_i^2}{n_0},$$

and allows one to calculate the concentration of donor impurity atoms.

2.7 Silicon Crystal Structure

This section is based on *Semiconductor Physics and Devices: Basic Principles* by Donald A. Neamen[17].

Silicon is the most commonly used semiconductor material. Instead of a simple cubic shape, silicon has a diamond crystal structure. We consider the tetrahedral structure, outlined by red in figure 2.12, as the building block of the diamond structure.

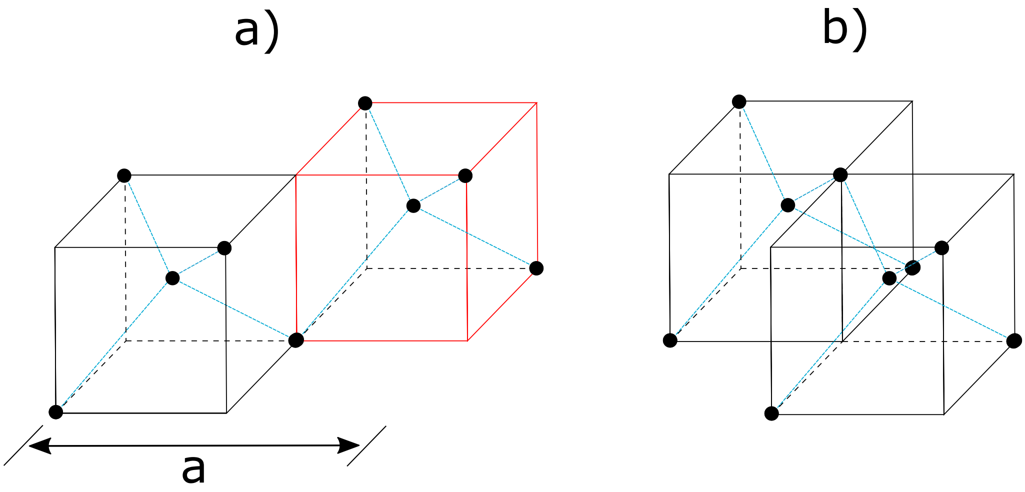

Figure 2.12. Tetrahedral building blocks, outlined in red, arranged in a manner such that if a) and b) are stacked on top of each other, the diamond structure is constructed.

By arranging the tetrahedral cells in the manner depicted in figure 2.12, and stacking 2.12 a) on top of 2.12 b), we obtain the diamond structure in figure 2.13.

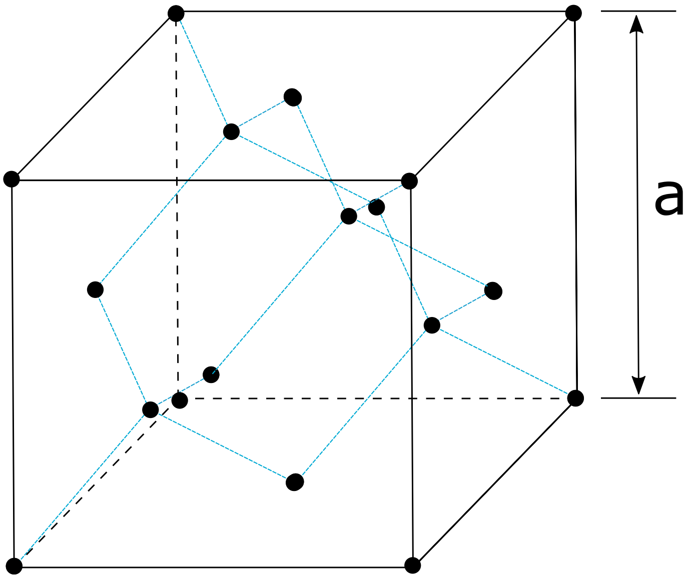

Figure 2.13. Silicon unit-cell, which exhibits the diamond-shaped structure. The unit cell contains 18 Si atoms.

2.7.1 Si(111) 7×7 reconstruction

When silicon is cut in the (111) direction, the resulting surface structure reconstructs itself into the Si(111) 7 × 7 structure. This surface reconstruction is most adequately modelled by the Dimer Adatom Stacked fault model, abbreviated as DAS, which is depicted in figure 2.14. The DAS model divides the 7 × 7 unit cell into two triangular subunits, each surrounded by 9 dimer pairs. These subunits separate the structure into the faulted and unfaulted sections. In each corner of the 7 × 7 cell, a corner-hole is formed, where the first three atomic layers are missing, as seen in the side view in figure 2.14. Each triangular subunit has 6 adatoms in the first layer, and 3 rest atoms in the second layer.

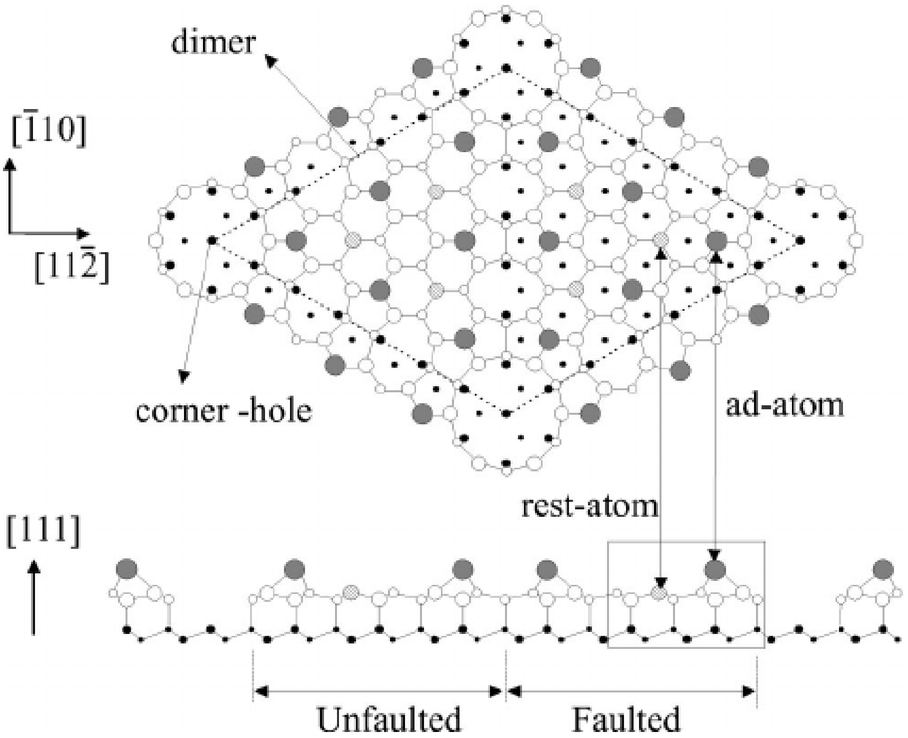

Figure 2.14. Top view and side view of the Si(111) 7 × 7 surface reconstruction as modelled by the DAS model. The 7 × 7 unit cell is outlined by the dotted line on the top view. The unit cell is divided into the faulted and unfaulted triangular subcells, by the dimer pairs formed on the outline of the subcells. The dimer pairs are formed in the layer below the rest-atoms. The figure was created by Bengio *et al.*[19].

2.7.2 Si(111) $\sqrt{3} \times \sqrt{3}$-B

If boron is deposited on a clean Si(111) sample and heated to sufficiently high temperature, the Si(111) $\sqrt{3} \times \sqrt{3}$-B reconstruction is formed at the interface. This structure is not as well documented as the Si(111) 7×7 reconstruction, although there are publications investigating the $\sqrt{3} \times \sqrt{3}$ reconstruction with other metals, like $\sqrt{3} \times \sqrt{3}$-Ag by Hasegawa *et al.*[20], and $\sqrt{3} \times \sqrt{3}$-Al by Katayama *et al.*[21]. The description of the Si(111) $\sqrt{3} \times \sqrt{3}$-B, that will be presented here, is based on the explanation by Aldahhak *et al.*[11].

When boron interacts with Si(111) at the interface the Si(111) $\sqrt{3} \times \sqrt{3}$-B reconstruction emerges, as depicted in figure 2.15, where the key characteristic is the boron replacing the silicon atoms situated below the adatoms in the second layer.

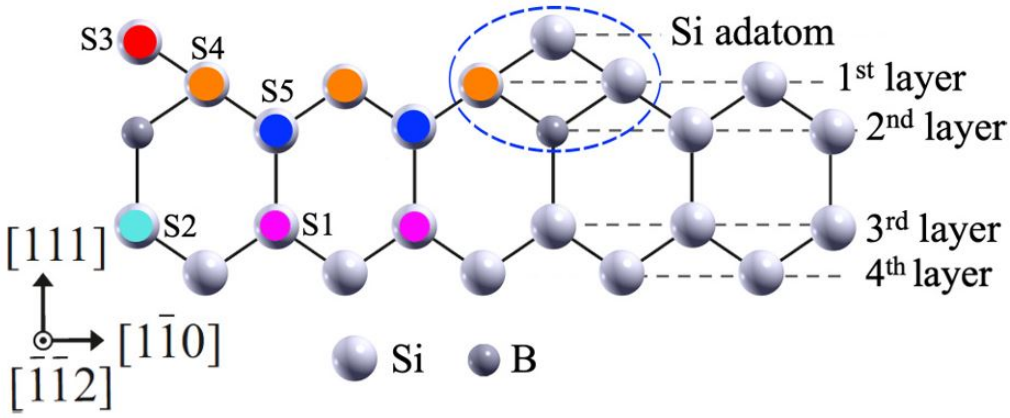

Figure 2.15. Side view of the Si(111) $\sqrt{3} \times \sqrt{3}$-B reconstruction. This reconstruction occurs as boron atoms replace the silicon atoms in the second layer, below the Si adatoms. The resulting surface states $S_1 - S_5$ that arise due to the reconstruction are marked by colours. The figure was made by Aldahhak *et al.*[11].

The reconstruction of the surface give rise to the occurrence of specific surface states, which are denoted $S_1 - S_5$ in figure 2.15. According to Aldahhak *et al.*[11], S_1 arises due to Si atoms in the third layer binding to Si atoms in the second layer, while S_2 occurs due to Si atoms in the third layer binding to the boron substituted atoms in the second layer. The S_3 surface state originates from the Si adatoms, while the S_4 and S_5 states comes from Si atoms in the first and second layer respectively.

Experimental 3

3.1 E-beam Evaporator

This section is based on *Dual Electron Beam Evaporator: Operating Manual* by Tectra[22].

The E-beam evaporator used to deposit boron onto silicon in the LEED/AUGER and XPS experiments is the Tectra e-flux2 e-beam evaporator. A side view schematic of the evaporator is presented in figure 3.1. The multiport (CF35) flange allows for loading two different deposition materials at the same time. The crucible is mounted on a rod holder close to the exit of the evaporator. The rods can be manipulated to change the distance of the crucible to the exit. The water cooled copper block provides cooling from an external source during deposition. Close to the exit of the evaporator, a flux sensor is mounted. Finally, after the exit of the evaporator, the shutter is located.

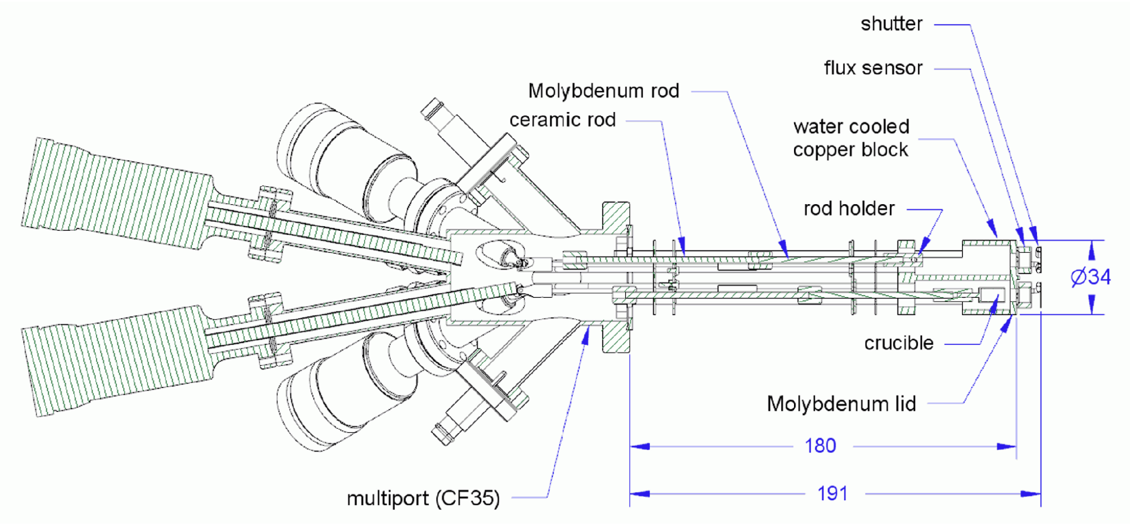

Figure 3.1. Side view schematic of the e-flux2 e-beam evaporator. The crucible which is the source of evaporant, is water cooled by the copper block during deposition. The flux sensor monitors the ion current, which enables for stabilization of the deposition rate. Finally the shutter, ensures that evaporant does not leave the e-beam evaporator before the right conditions are set. This shematic is from the Tectra manual[22]

The most crucial components in creation of evaporant during deposition is shown in the close up image of the crucible in figure 3.2. The dotted lines outline the tungsten filament wire, that encircles the crucible. The first step to the evaporation process, is generating a current through the tungsten filament, causing it to release electrons as it heats up. A high potential difference is applied between the tungsten filament and the crucible, which forces the released electron to move toward the crucible. This electron bombardment heats the crucible to a point where evaporation starts occurring. This flux of evaporated atoms is called an emission current.

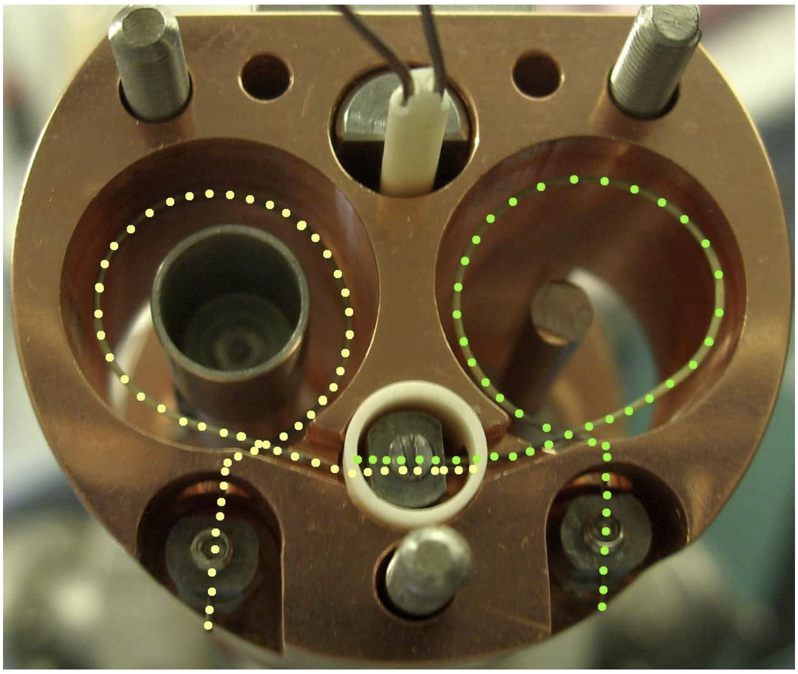

Figure 3.2. Close up of the e-beam evaporator showing the crucible surrounded by the tungsten filament outlined by the dotted lines. This image is taken from the Tectra manual[22]

As boron is released from the crucible, some of the electrons coming from the filament might ionize the evaporant atoms, and when these ions pass the flux monitor electrode in figure 3.1, it induces a current, called the ion current. Since electrons are also present in the vicinity a negative bias of usually −24 V is applied to the flux sensor to repel electrons. This ensures that only the evaporant ions influence the ion current. The ion current is used to stabilize and monitor the deposition rate of the e-beam evaporator. It is therefore important to ensure that the evaporator is sufficiently outgassed, as other residual gasses still present might also get ionized.

During our experiments the ion current was kept at 50 nA while depositing and the emission current ranged from 11-14 mA. Both were kept as constant as possible during each deposition and the emission current increased between depositions.

3.2 Setup LEED and AES

This section is based on *Rear View Leed With Model 8011 Electronics Operating Manual* by Thermo VG Microtech[23].

All LEED and AES experiments were performed using the Rear View LEED with model 8011 electronics from Thermo VG Microtech. The setup was mounted on a vacuum chamber under UHV conditions.

The two main components composing the RVL setup is the electron gun and the mesh assembly with a phosphor screen attached. The basic concept of the setup is that the electron gun focuses an electron beam onto the sample. The diffracted electrons then impinge on the mesh assembly and the electrons that pass through are collected by a phosphor screen. The phosphor screen then fluoresces where electrons strike, creating the LEED pattern that can be observed through a viewport on the rear of the setup.

In AES mode the screen collects the electrons and the resulting current is measured to obtain the AES spectra. A schematic of the setup can be seen in figure 3.3.

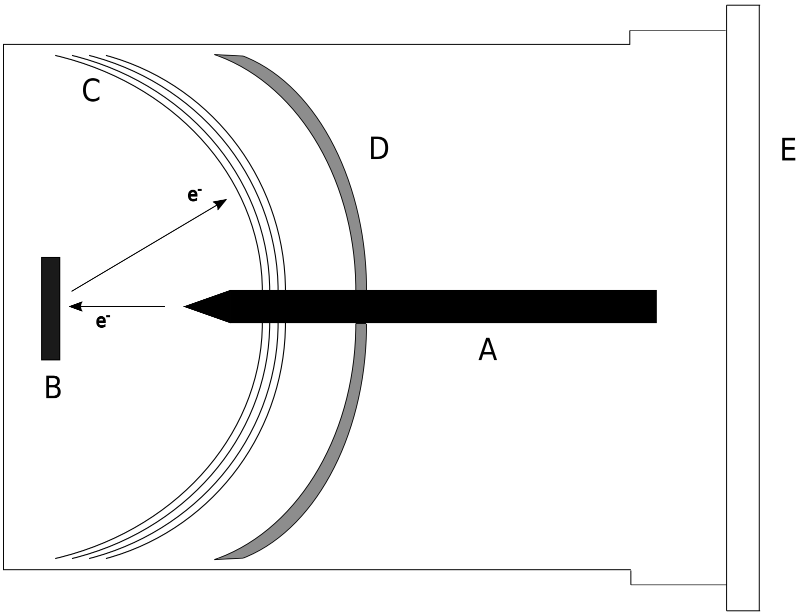

Figure 3.3. Main components of the Auger/LEED setup. **A** The electron gun emits electrons and accelerates them towards the sample **B**. The electrons are diffracted towards the mesh assembly **C** and the ones that pass collide with the phosphor screen **D**. The LEED pattern can then be observed from the rear part of the setup through the viewport **E**.

3.2.1 Electron Gun

The electron gun creates an electron beam with energy ranging from 5 V to 1000 V for LEED and up to 3000 V for AES. A filament which is at a negative potential with respect to earth emits electrons. These electrons are accelerated and focused into a beam by potentials over different elements between the filament and the outlet of the electron gun.

3.2.2 Mesh Assembly

The mesh assembly works as to prevent inelastic scattering. This is achieved by applying a negative potential to one of the meshes. This potential is slightly more positive than the energy of the electron gun. In this way the number of inelastically scattered electrons is reduced and the mesh works as a retard mesh.

The screen is held at a potential of approximately +5 kV. Diffracted electrons with energies higher than the retard mesh will pass through and strike the screen which detects the electrons and obtains the Auger signal or LEED pattern depending on the which operating mode is selected.

3.2.3 Shield

When the e-beam evaporator is mounted on the Auger/LEED setup it is possible to cover part of the sample behind a shield. While shield and evaporator positions are fixed the sample is mounted on a 4D-manipulator allowing us to freely cover parts of the sample that should remain clean while depositing. The sample-shield-evaporator setup enables us to produce the boron wedge sample discussed in section 4.2 and is sketched in figure 3.4.

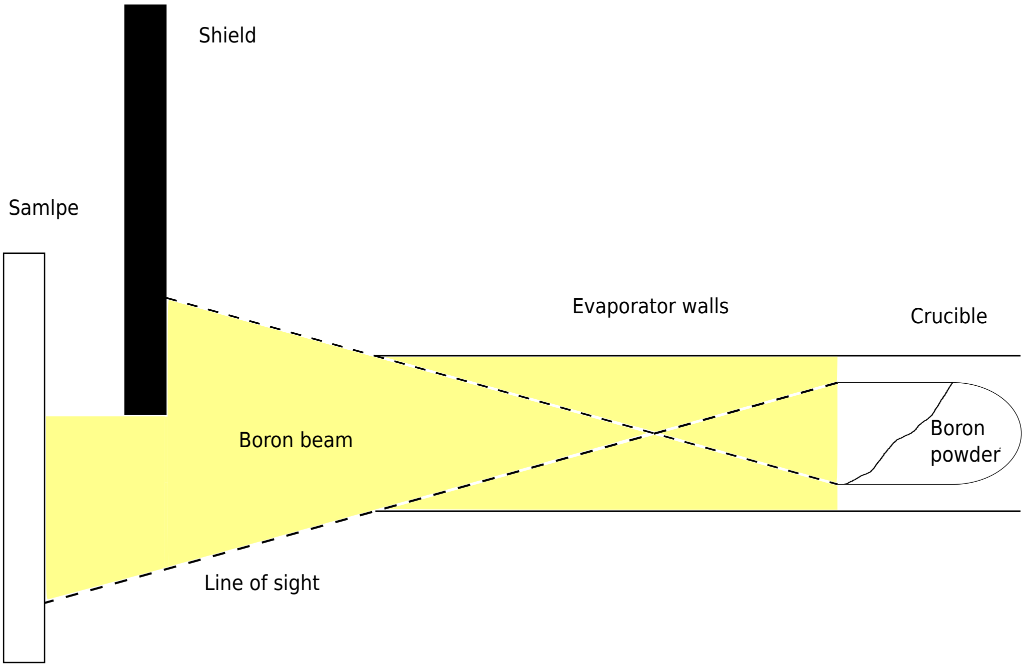

Figure 3.4. Sketch of the sample-shield-evaporator setup. Part of the moveable sample is covered behind the shield allowing us to produce a boron wedge.

3.3 Setup ASTRID2

3.3.1 ASTRID2 Storage Ring

This section is based on *ASTRID2: THE ULTIMATE SYNCHROTRON RADIATION SOURCE* by ISA[24].

The MATline beamline used in conducting the XPS experiments during this project, is one of 7 beamlines at the ASTRID2 synchrotron facility, at the Department of Physics, Aarhus Univerity. The ASTRID2 storage ring, depicted in figure 3.5, consists of 6, 2.7 m long straight segments and 6 arcs to form a ring-like tube, with a circumference of 45.7 m. Four of the beamlines originate from insertion devices, while the remaining 3 are formed by bending magnets. The storage ring circulates electrons with energy 580 MeV at a current of 180 mA. One of the main objectives of the ASTRID2 synchrotron, is providing a very brilliant light source. To achieve this, combined-function magnets consisting of a combination of dipole, quadruple and sextupole magnetic fields all-in-one, are utilized to obtain a very small emmitance of 12 nm, resulting in a beam-size of 200×25 microns in the straight segments.

To maintain this current as synchrotron radiation is emitted, the ASTRID2 ring receives a top-up of electrons from the ASTRID ring, located in an adjacent room, periodically. Essentially, electrons are produced at 100 MeV externally, followed by injection into the ASTRID ring. The ASTRID storage ring effectively functions as an electron booster. By ramping the energy of the circulating electrons to 580 MeV, matching the energy in the ASTRID2 ring, the ASTRID ring can provide electrons at the required energy through an injection tube.

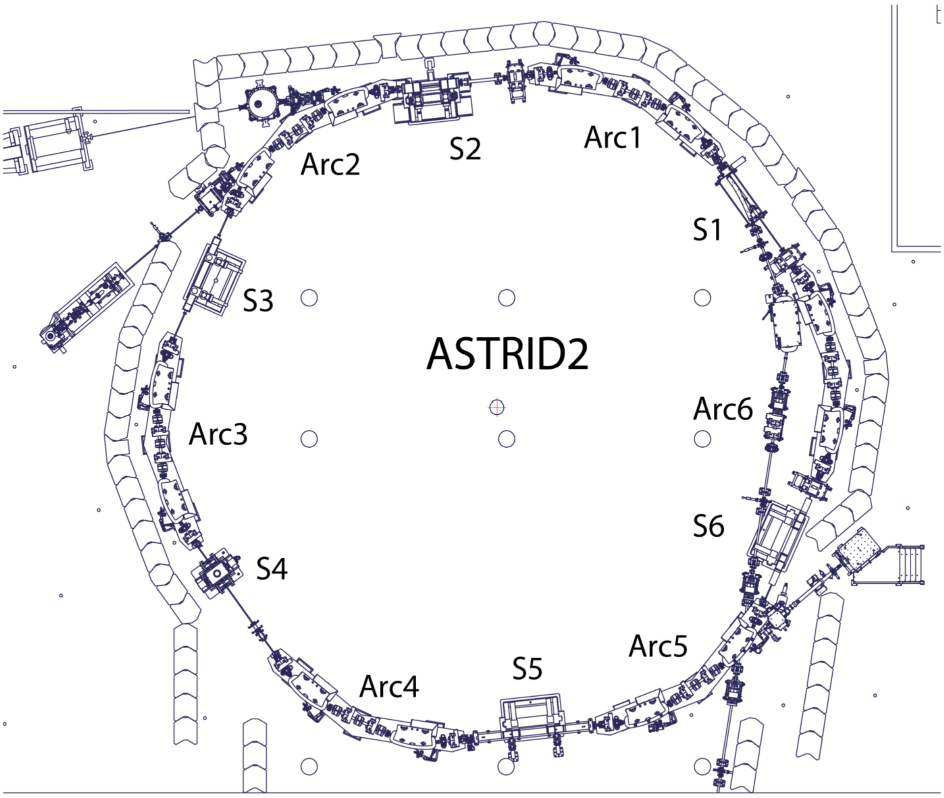

Figure 3.5. Schematic overview of the ASTRID2 storage ring. The storage ring consists of 6 straight segments, denoted by S1-S6, and 6 arcs marked by Arc1-Arc6. Bending magnets are mounted on every arc, leading to synchrotron radiation when an external magnetic field bends the trajectory of circulating electrons. The MATline beamline, which the XPS system used in this project was mounted on, produced photons by means of a wiggler connected to the S2 segment of the ASTRID2 storage ring. The storage ring is surrounded by concrete to shield users from stray radiation. To maintain the energy of electrons in the storage ring, the ASTRID ring, located in an adjecant room, provides electron to the ASTRID2 ring in the so-called top-up process. This schematic is adapted from ISA[24]

3.3.2 MATline

The AU-MATline breamline is a material science beamline. It is ideal for performing surface science techniques at UHV conditions. This includes the PHOIBOS 150 system we used to conduct our XPS measurements. The photon source of the AU-MATline, is generated by a 0.7 m long 2T multipole wiggler mounted on the S2 segment, seen in figure 3.5. The synchrotron radiation generated by the wiggler passes through a SX-700 monochromator, allowing for the selection of specific photon energies. The optimal range of usable photon energy is in the range 20 eV - 700 eV, but can be used at up to 1000 eV.

3.4 XPS Hemispherical Analyzer

This section is based on the *PHOIBOS 100/150 Manual*[25].

For the XPS experiments conducted at the AU-MATline beamline, we used the PHOIBOS 150 hemispherical analyzer, depicted in figure 3.6. The analyzer has a mean radius $R_0 = 150$ mm, which is the distance from the center of the hemispheres to the electrons path trough analyzer. The inner hemisphere has radius $R_{inner} = 0.75$ mm , while the outer hemisphere has radius $R_{outer} = 1.25R_0 = 187.5$ mm.

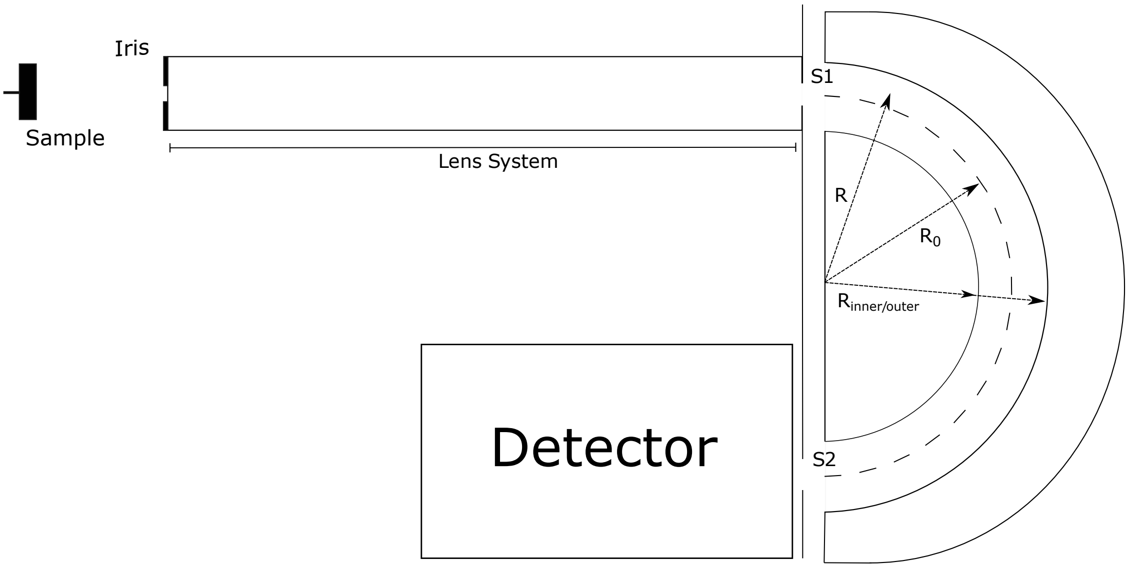

Figure 3.6. Schematic of the PHOIBOS 150 hemispherical analyzer. Electrons are focused by the lens system, whereafter they pass though the entrance slit $S1$ and exit slit $S2$ of the hemispheres, into the detector. R_{inner} and R_{outer} are the radii of the inner and outer hemispheres, respectively. R_0 is the distance from the center of the hemispheres to the central path through the analyzer, while R is the distance to the average electron path.

3.4.1 Pass Energy

An electrostatic field is generated across the two hemispheres, by applying a potential difference between them. This results in a radial dependence $E \propto \frac{1}{R^2}$, for electrons passing through the analyzer in a path, with distance R from the center of the hemispheres. For photoelectrons to pass through the analyzer and into the detector, they must not deviate too far from the nominal electron path, outlined by the dotted line in figure 3.6. Thus, electrons can not posses too much or too little energy, such that their trajectory deviates too far. This allowed range of deviation from the nominal electron path is determined by the pass energy the analyzer.

3.4.2 Spectral Linewidth

On a given XPS spectrum obtained from the hemispherical analyzer, the observable transition peaks will have a lineshape and a linewidth. Electronic transitions have a natural linewidth, which occurs due the natural lifetime of a transition. But in addition the XPS peaks experience further broadening effects due to analyzer and the photon source. This means that the total linewidth is a combination of all of these broadening effects. In reality, the contributions to the total linewidth can also come from different types of lineshapes, but we can approximate it by assuming all contributions are Gaussian in nature

$$\Delta E = \sqrt{\Delta E_{an}^2 + \Delta E_{level}^2 + \Delta E_{photon}^2},$$

where ΔE_{level} is the natural linewidth of a given transition, ΔE_{an} is the broadening due to the analyzer, and ΔE_{photon} is the broadening due to the photon source.

3.4.3 XPS Setup

For the actual experimental XPS setup used at the ASTRID2 synchrotron, the PHOIBOS 150 hemispherical analyzer was mounted on a UHV chamber, which the AU-MATline beamline was also connected to, providing the photon radiation source. A simplified sketch of the experimental setup is shown in figure 3.7.

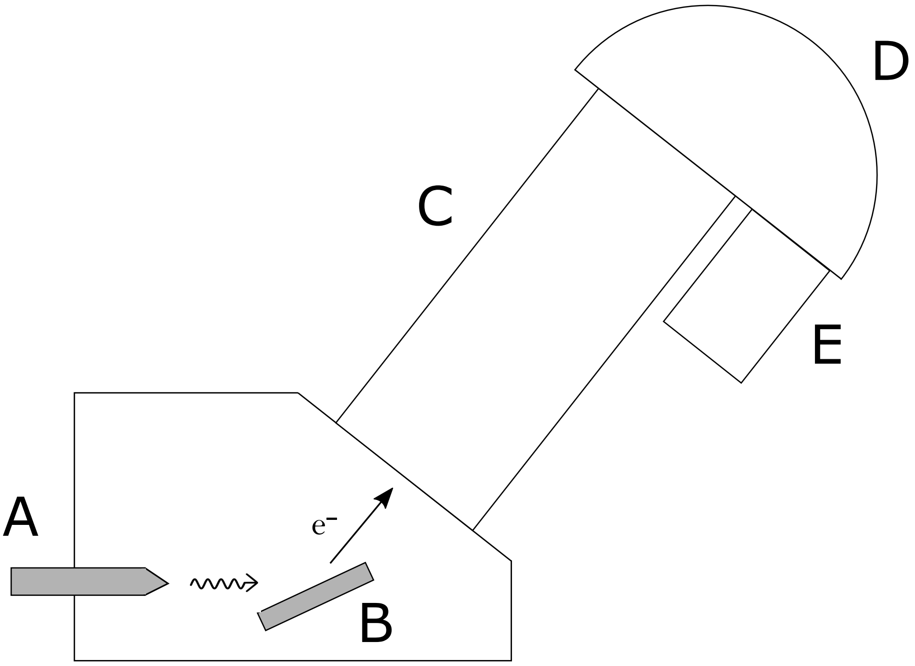

Figure 3.7. A simplified schematic of the XPS experimental UHV setup connected to the AU-MATline beamline at ASTRID2. **A** is the synchrotron radiation source. **B** is the sample. **C** is the lens system used in focusing the beam of photoelectrons, into the hemispherical analyzer, denoted by **D**. Then the electrons are finally detected by DLD-detector, marked by E.

For all XPS measurements made during the experiment at the beamline we used the following analyzer settings:

- **Entrance Slit:** $3 : 3 \times 20$(curved)
- **Exit Slit:** B:Open
- **Iris Diameter:** 60 mm
- **Measurement Mode:** FAT
- **Pass Energy:** 100 eV
- **Lens Mode:** LAD

These settings were used, as they yield the best result based on experience of the supervisor of the AU-MATline beamline.

Results and Discussion 4

Deposition of boron at sufficiently high temperature results in formation of the Si(111) $\sqrt{3}\times\sqrt{3}$-B reconstruction as is documented in various publications[26][27]. The most widely used method for creating a boron layer on top of silicon is to anneal boron doped silicon which, brings boron to diffuse onto the surface of the sample of investigation. This process can not take place at room temperature since annealing by definition occurs above room temperature. Thus to investigate how boron layers arrange on a clean Si(111) surface, at room temperature, deposition must be considered. To our knowledge, deposition of boron on Si(111) has not earlier been performed. Thus we deposit boron on silicon both at room temperature and at 450°C to compare the results. All LEED, Auger and XPS measurements were conducted under UHV conditions in a pressure of $5 \cdot 10^{-10}$ mbar or better.

4.1 LEED Si(111)

As described in section 2.2, LEED patterns are highly sensitive to the quality and cleanliness of a surface under investigation. Therefore we used LEED partly to verify that the our sample was clean but also to confirm that we indeed were investigating the Si(111) surface and that the deposited boron would show the expected characteristics.

4.1.1 Si(111) 7×7 Reconstruction

Before any deposition when using the Auger/LEED setup we qualitatively verified the cleanliness of the Si(111) surface by confirming that we had a clear image of the Si(111) 7×7 reconstruction, as the one seen in figure 4.1. This LEED image showcases the 1×1 bulk-like pattern which consists of 6 very bright spot (of which one is covered behind the electron gun in the middle). One of these is encircled by a red circle in to bottom of the image for clarity. Between each pair of these 1×1 spots we can see 6 additional but less prominent spots that divide the line between the 1×1 spots, into 7 regions indicating the 7 unit cells that the 7×7 reconstruction consists of on each side. These spots are encircled by the red ellipse to the right. Furthermore features known from the 7×7 reconstruction can be seen just around the electron gun, which appears as the dark shadow in the center of the image.

To obtain this image an electron energy of 54 eV was used. The literature gives examples of different electron energies that give rise to this LEED pattern. Common for all is that this LEED pattern occurs at low electron energies e.g. Levin *et al.*[28], who state that the pattern arises at 40 eV. This discrepancy can at least partly be explained by the fact that the different LEED patterns are visible at a range of electron energies. During our experiments electron energies between 49 eV and 54 eV enabled us to obtain similar images. When searching for LEED patterns the electron energy is swept over a range of energies and the spots on the phosphor screen comes and goes continuously increasing or decreasing in intensity when the electron energy changes.

For our experiments, it was not important at which electron energies exactly the LEED patterns arose since our use of LEED was merely qualitative and only used to determine whether the sample was clean or not.

Figure 4.1 shows a LEED pattern that only arises on a sample surface that is very clean. When a less clean sample was investigated we would only see the 1×1 pattern. If only the 1×1 pattern appeared we could usually anneal the sample forcing adsorbates to abandon the surface, leaving behind a clean 7×7 reconstruction.

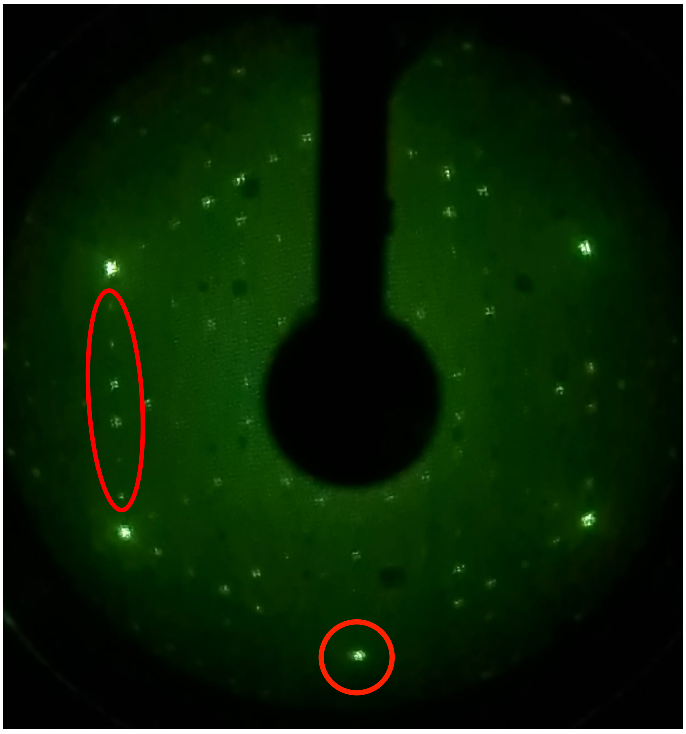

Figure 4.1. LEED image of the Si(111) 7×7 reconstruction. Brighter spots shows the 1× pattern indicated by a red circle in the bottom of the image. To the left the red ellipse shows the position of the less prominent spots arising due to the 7×7 reconstruction. The image was obtained at an electron energy of 54 eV.

4.1.2 Boron Deposition onto Si(111) at 25°C and 450°C

During the investigation of the temperature criterion for producing the Si(111) $\sqrt{3}\times\sqrt{3}$-B reconstruction we found that depositing boron on a clean Si(111) surface at room temperature did not result in the Si(111) $\sqrt{3}\times\sqrt{3}$-B reconstruction, since the expected LEED pattern according to the literature[29] did not arise. This is supported by our XPS experiments processed in section 4.5.4.

Instead, we increased the temperature of the sample during deposition to 450°C to observe the effect. This experiment was performed on a sample that did not present a perfect

Si(111) 7 × 7 reconstruction as desired prior to the deposition. The 1 × 1 pattern was visible but the LEED image lacked many features of the Si(111) 7 × 7 reconstruction. Even annealing the sample multiple times did not result in a perfect LEED pattern.

By depositing boron at 450°C onto this sample, we obtained the LEED pattern shown in figure 4.2. In this image the 1 × 1 pattern spots, in the red circle, are not as well-defined as is the case in figure 4.1. The same is the case for Si(111) 7 × 7 reconstruction spots in the red ellipse where only weak remnants are visible. The Si(111) $\sqrt{3} \times \sqrt{3}$-B reconstruction spots, marked by the yellow circle, are smeared out showing that the reconstruction is not perfect. We have two possible explanations for this behaviour. Either the insufficiently ordered Si(111) sample before deposition resulted in boron settling on the surface in a less ordered structure, giving rise to this half/half image. The other reason can be that the temperature of the sample while depositing was simply too low for creation of the Si(111) $\sqrt{3} \times \sqrt{3}$-B reconstruction to occur properly as was the case when depositing at room temperature.

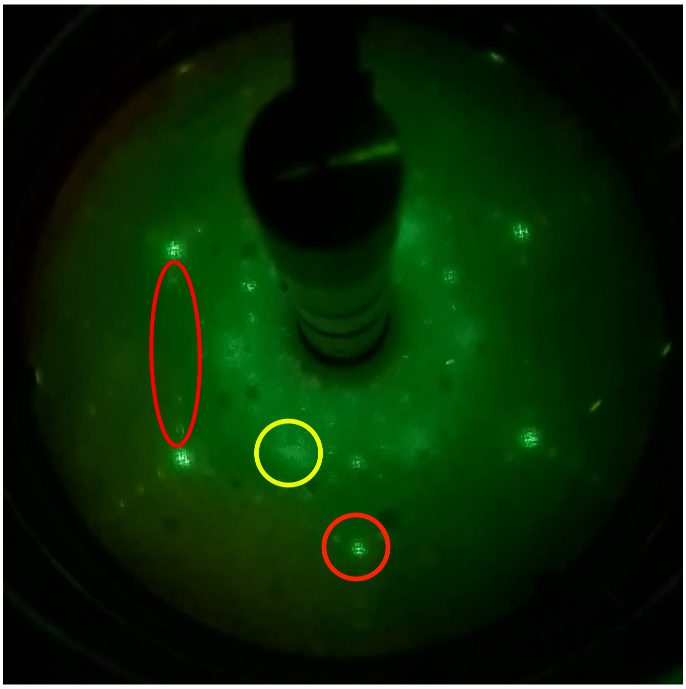

Figure 4.2. LEED image of the Si(111) $\sqrt{3} \times \sqrt{3}$-B reconstruction. Most prominent spots shows the 1×1 patter indicated by a red circle in the bottom of the image. The smeared spots indicated by a yellow circle shows the $\sqrt{3} \times \sqrt{3}$ reconstruction. To the left the red ellipse shows weak remnant spots of the 7×7 reconstruction. The image was obtained at an electron energy of 54 eV.

4.1.3 Annealing Si(111) Post Deposition

We had earlier experienced that we could not fully clean a Si(111) surface once boron was deposited. Annealing a boron deposited Si(111) sample always resulted in creation of the Si(111) $\sqrt{3} \times \sqrt{3}$-B reconstruction identical to the LEED pattern seen in figure 4.3, where the 1 × 1 pattern is marked by a red circle, the $\sqrt{3} \times \sqrt{3}$ reconstruction is indicated by a yellow circle and the Si(111) 7 × 7 reconstruction is now gone. We ascribe this behaviour to strong bonding of the boron in the Si(111) $\sqrt{3} \times \sqrt{3}$-B interface.

In an attempt to clean a boron deposited Si(111) surface we found that the bonding is in fact so strong that multiple subsequent annealing cycles of 30 seconds at 1000°C would cause the silicon crystal to degrade before the boron leaves the sample.

The LEED image in figure 4.3 was obtained by annealing the same sample that is depicted in figure 4.2 for 30 seconds at 1000°C. This shows that the Si(111) $\sqrt{3}\times\sqrt{3}$-B reconstruction can easily be created at sufficiently high temperatures even though the original Si(111) surface was imperfect.

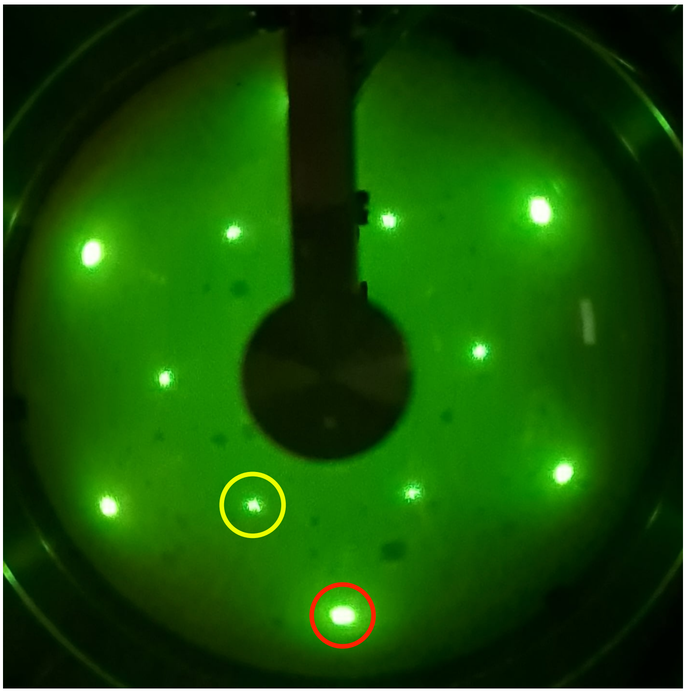

Figure 4.3. LEED image of the Si(111) $\sqrt{3}\times\sqrt{3}$-B reconstruction. Most prominent spots shows the 1×1 patter indicated by a red circle in the bottom of the image. The 6 spots forming a smaller 30° rotated hexagon indicated by a yellow circle shows the $\sqrt{3}\times\sqrt{3}$ reconstruction. The image was obtained at an electron energy of 54 eV.

4.2 Auger/LEED spotsize

In order to know the size of the scanned area when performing AES and LEED experiments we determined the spatial resolution of the setup by using the knife-edge method, as described in the following.

On a clean Si(111) sample, that was annealed for 30 seconds at 1010°C we deposited boron at around $T \approx 500$°C for 5 minutes. One part of the sample was covered by a shield to prevent exposure to boron when depositing on the uncovered part of the Si(111) sample. We made multiple Auger scans of the Si signal at 92 eV starting at a position on the sample where a clear LEED image of the Si(111) 7×7 surface reconstruction was visible. This continued in increments of 0.1 mm until a position where the LEED pattern of Si(111) $\sqrt{3}\times\sqrt{3}$-B was observed. By plotting the intensity of the Si signal as a function of the lateral position and fitting the Gaussian error function

$$f(x) = \frac{1}{2}\left[1 + \mathrm{erf}\left(\frac{x-\mu}{\sigma\sqrt{2}}\right)\right],$$

where μ is the position and σ is the standard deviation we obtain the fit in figure 4.4.

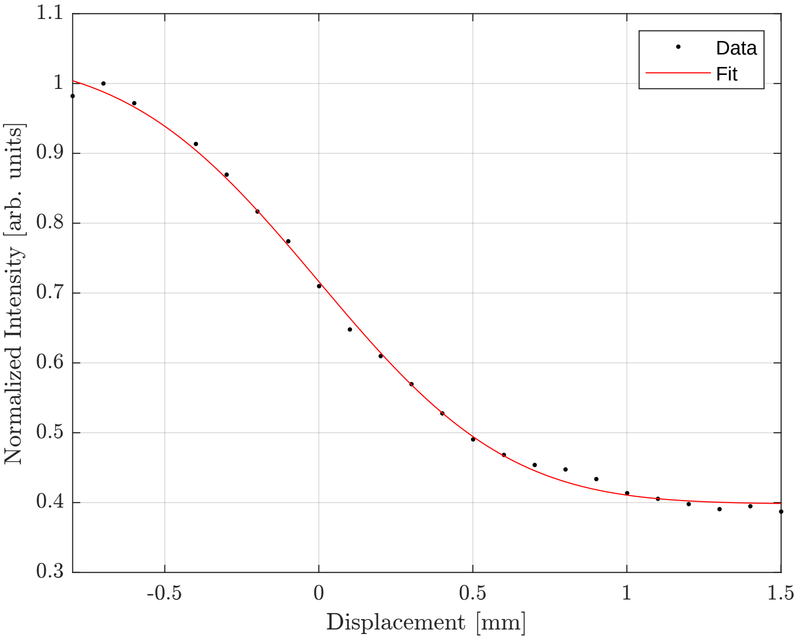

Figure 4.4. Intensity of the Si signal as a function of the displacement over the transition from a clean Si(111) surface to the boron deposited B/Si(111) surface.

Since the error function fits well to the data this indicates that the Si signal indeed acts as an error function when we scan over the transition from the clean Si surface to the boron deposited part of the sample.

By performing numerical differentiation on the fit of the error function in figure 4.4 the Gaussian distribution in figure 4.5 was obtained. The full width at half maximum (FWHM) was determined to $\Delta W = 1.16$mm which is our measure of the spot size.

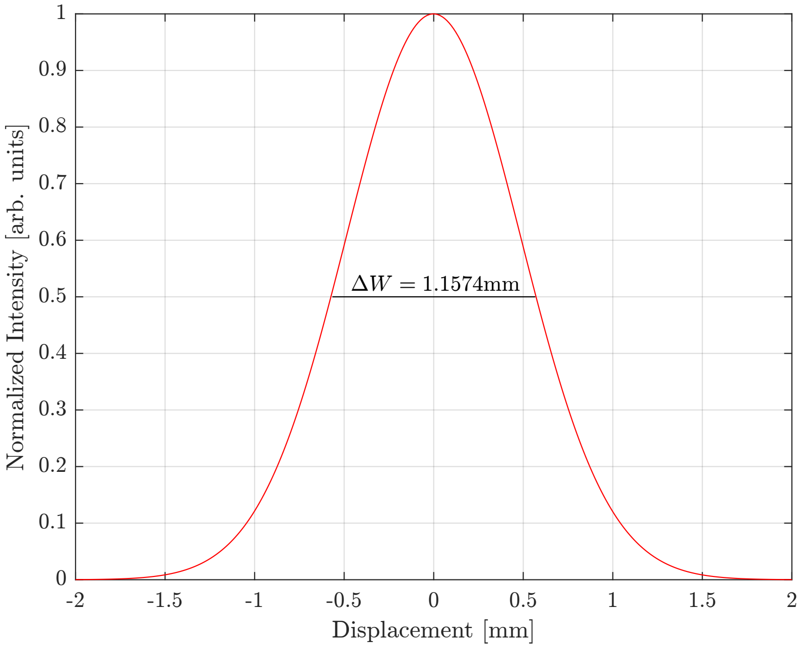

Figure 4.5. Gaussian distribution emerging from differentiating the error function in figure 4.4. The FWHM corresponds to the spotsize of the electron beam used in the AES setup.

In the following experiment we are depositing a wedge-like step structure of boron (B-wedge) on Si(111) by first depositing a layer of boron and subsequently depositing another layer but now covering part of the sample so that the additional boron will only be deposited on one part of the sample and so on, as seen in figure 4.6. For a B-wedge sample like this a small spot size lower than the width of the steps is desirable as this would enable one to make measurements on only one thickness of the deposited boron. Hence measuring over the step edge will lead to performing measurements where the thickness of the boron layer is ill-defined.

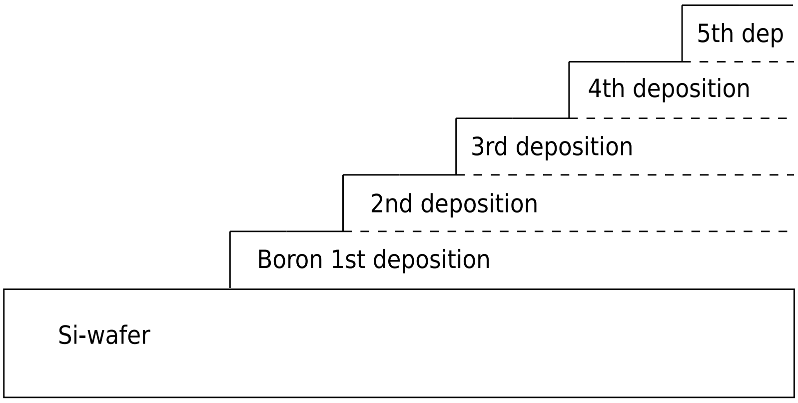

Figure 4.6. Schematic drawing of a wedge-like boron structure deposited on a clean silicon sample.

4.3 Deposition Rate of Boron on Si(111) at Auger System

In order to investigate the interface between boron and Si(111) we wanted to be able to control the deposition rate of the evaporator accurately. By depositing a boron wedge on Si(111) as described in section 3.2, we could investigate how the silicon and boron signals changed with increasing boron thickness. While depositing boron the sample was displaced in increments of $\frac{1}{2}$ mm every 30 seconds for a period of 14 minutes leaving approximately 5 mm of the Si(111) sample clean. The growth temperature, the temperature of the sample while depositing (T_g), was set to room temperature.

Auger spectra were subsequently obtained at different positions by displacing the sample, and thereby the scanned area in increments of 1 mm. The measurements were taken over the energy range 40-350 eV with a step size of 1 eV. In this way we would initially make scans at positions on the sample where we detected pure Si(111) which was confirmed by a LEED image of the Si(111) 7×7 reconstruction. As the sample was displaced we should detect a weaker and weaker Si signal and an increasingly stronger boron signal as a result of the increasing thickness of the deposited boron. This enabled us to produce the growth curves seen in figure 4.7.

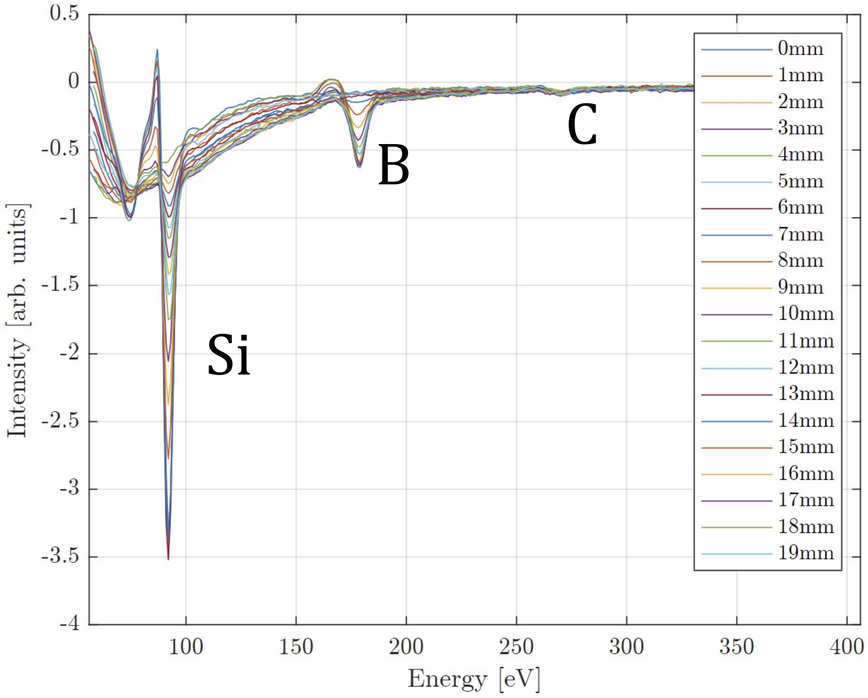

Figure 4.7. Multiple Auger scans over the surface of the B-wedge sample. As more boron is deposited the increasingly thicker layers of boron intensifies the boron signal and the Si signal vanishes. The Auger spectra were obtained at an electron energy of 2 keV.

In XPS, the peaks would be fitted to a specific line-shape corresponding to the observed transitions and the areas of these peaks could then be used as a measure of the intensity of the signal. This is not a possibility in AES due to the nature of the differentiated spectrum. Furthermore, between scans at different positions on the sample i.e. different thicknesses of the deposited boron the baseline would change as seen in figure 4.7 which further complicates the analysis. As a measure of the intensity we therefore used the difference between the maximum and the minimum values of the Auger signal as visualized i figure 4.8.

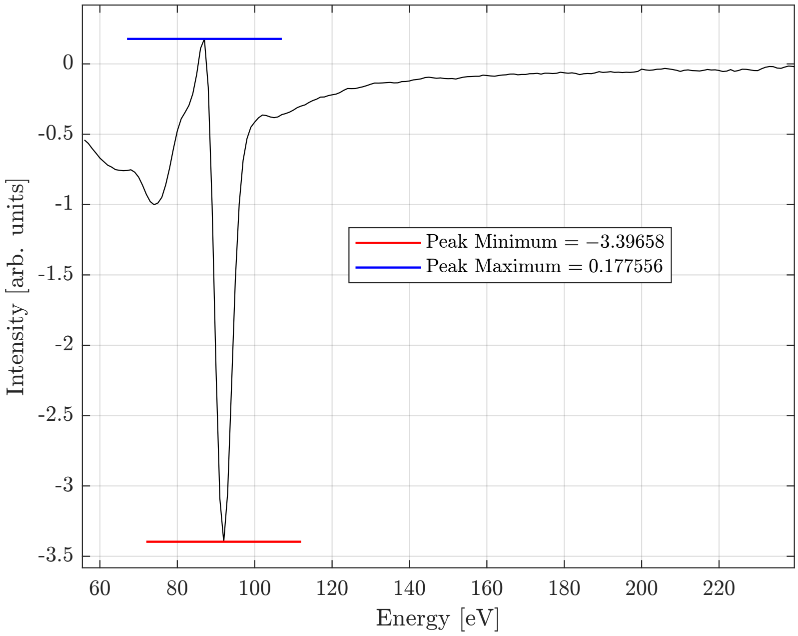

Figure 4.8. Spectrum of the main Si signal at 92 eV (minimum). The intensity of the peak found as the difference between minimum (red line) and maximum (blue line) of the AES signal. The Auger spectrum were obtained at an electron energy of 2 keV.

The calculated intensities were then plotted against deposition time and fitted to an exponential function of the form $f(x) = a \cdot \mathrm{e}^{-bx}$, where a is the maximum intensity i.e. the intensity of an element measured on a clean and pure surface and b is the absorption coefficient. This fit can be seen in figure 4.9.

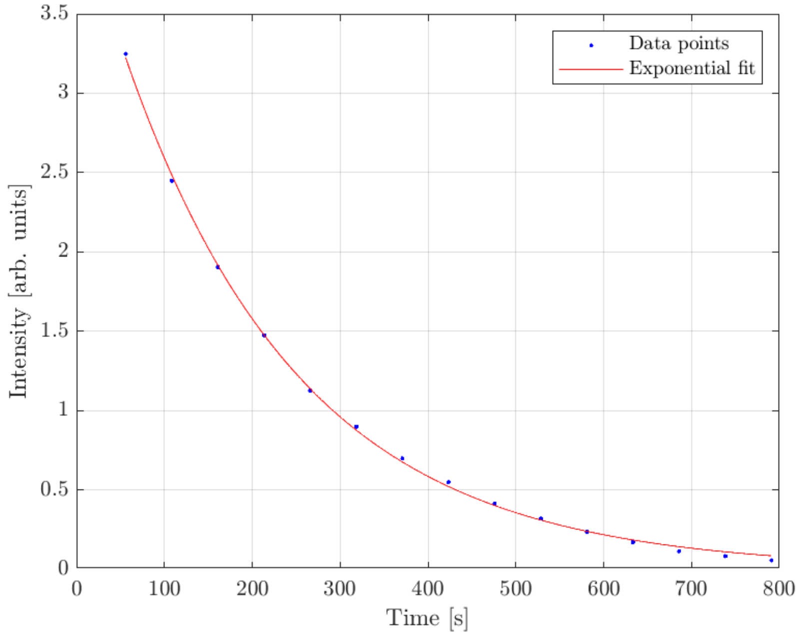

Figure 4.9. Intensity of the Si signal as a function of the time deposited. The signal decreases exponentially with time due to the increasingly thicker boron layer deposited.

The data fits the exponential very well as expected from the Lambert-Beer law 2.5 with a RSME of 0.0084. The value of the absorption coefficient is found to be 0.004959. The inelastic mean free path (IMFP) for boron at the electron energy of interest is a measure of the thickness of boron that will halve the measured intensity. By combining the absorption coefficient and the IMFP, the deposition rate is found

$$\text{Deposition rate} = \frac{IMFP}{\text{Attenuation time}} = 6.04\text{Å} \Bigg/ \frac{(0.004959 \text{ per second})^{-1}}{60 \text{ seconds/minute}} = 1.797\text{Å/min.}$$

4.3.1 Depostion at Room Temprature

At room temperature we made 13 depositions on the Si(111) sample. We started out slowly, only depositing very thin layers of boron in order to make sure that we would not miss details about the B-Si interface by depositing too much. The duration of these depositions were 1, 1, 1, 1, 2, 2, 4, 4, 8, 8, 16, 16 and 32 minutes in this sequence. The first 3 depositions on this sample were performed directly after each other while the rest of the series was created approximately 12 hours later. Spectra were recorded immediately after each deposition. The pressure in the UHV chamber during deposition was monitored and always started between $4 \cdot 10^{-9}$ and $5 \cdot 10^{-9}$ mbar, but for the longer depositions we observed that the pressure increased to $1.3 \cdot 10^{-8}$ mbar after about 10 minutes, which we expect is due to degassing.

Spectra of the Si2p, B1s, O1s and C1s recorded as well as valence band spectra. Additionally, survey spectra were obtained prior to any measurement series in order to make sure that the full spectrum behaved as expected.

4.3.2 Deposition at 450°C

To compare how increasing the sample temperature while depositing affected the interface between Si(111) and boron we also deposited at a sample temperature of 450°C on a second clean Si(111) sample. In the setup at ASTRID2 the sample temperature is measured by a thermocouple that is connected to the back side of the sample holder. Hence the measured temperature deviates from the actual temperature of the sample. Out of experience, the staff approximates the temperature deviation to be around 50°C. We decided to set the temperature to 680 K, equivalent to 403°C. Since the temperature measured should be 50°C lower than the actual temperature of the sample we arrive approximately at $T = 450°\text{C}$. This temperature is stable at a filament current of I=5.2A.

During deposition on the first sample at room temperature, we experienced degassing which occurred at different rates at different stages. Initially, when depositing for more than approximately 10 minutes, we had observed an increase in the pressure in the vacuum chamber. This effect however vanished after some depositions. For the deposition of 32 minutes, a large increase in pressure also happened after approximately 20 minutes which left the sample contaminated by oxygen on the surface. For this reason we only performed depositions with a duration of less than 20 minutes. Hence, when we wanted to make longer depositions we divided depositions longer than 20 minutes into shorter intervals i.e. a deposition of 32 minutes was divided into 2 depositions of 16 minutes in between which we let the evaporator cool down to prevent degassing. The duration of the depositions on this sample were 1, 1, 1, 1, 2, 4, 8, 16, 16+16, 16+16, 32 minutes. It should be noted that there was a downtime of approximately 2 hours after the second deposition, due the beamline shutting down. Consequently, we had to calibrate the XPS scans taken before and after the shutdown, in order to compare them.

4.4 Deposition Rate of Boron at ASTRID2

The previous sections described the process of determining the deposition rate of the e-beam evaporator while mounted on the Auger/LEED UHV system in Aalborg. This section will detail the process of determining the deposition rate of the same evaporator, while mounted on the XPS system at the ASTRID2 MATline in Aarhus.

The measurements with the Auger system were made in preparation for the XPS experiments at ASTRID2. As stated previously, we wanted to have a controlled deposition rate when depositing at ASTRID2. In section 4.3 we were able to get a well controlled deposition rate, with a good fit to the Lambert-Beer Law. Thus, when depositing at ASTRID2 we again used an ion current of 50nA, as it had yielded nice results for the Auger measurements.

In the Auger/LEED UHV system, we were able to produce a boron wedge on the silicon sample, during a single continuous deposition. This was not possible in the XPS chamber. Instead, we had to deposit a layer of boron on the whole sample, make a scan, deposit, make a scan, etc.

To calculate the deposition rate, we need to determine how much weaker the Si2p signal becomes as we deposit boron. To do this, we used the area of the Si2p envelope as a measure of the intensity of the silicon signal. As mentioned in section 4.3, for XPS measurements we are able to accurately determine the area of the Si2p XPS envelope by fitting multiple peaks to the Si2p envelope. This was done in SpecsLab Prodigy and CasaXPS. From the areas determined there we were then able to create growth curves, by plotting these areas against the deposition time.

4.4.1 Depostion at Room Temprature

We now fit the growth curves to the exponential function $f(x) = a \cdot \mathrm{e}^{-bx}$, as we did in section 4.3, to determine the absorption coefficient b. This results in the fit depicted in figure 4.10.

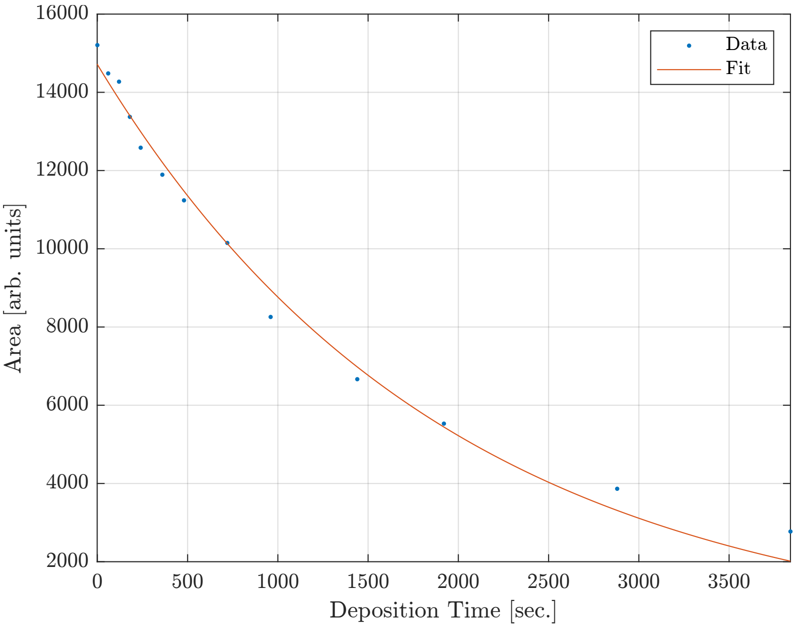

Figure 4.10. Evolution of the Si2p peak area as boron is being deposited for increasingly longer times. Boron was deposited at room temperature. The XPS scans where made at excitation energy $h\nu = 180$ eV.

The fit shows good correlation with the data, especially at shorter deposition times. Although, for longer depositions it is apparent that there is significant deviation between the data and fit, as reflected in the RMSE of 0.0484. Even though the fit is significantly worse than the Auger fit in section 4.3, with a deviation in the RMSE of around 6 times more, the relationship between intensity and deposition time described by the Lambert-Beer law is still clear. The binding energy of the Si2p transition is approximately 100 eV, and the excitation energy is 180 eV, resulting in the kinetic energy $E_k = E_{exc} - E_b = 180 \text{ eV} - 100 \text{ eV} = 80$ eV. The IMFP of Si2p at $E_k = 80$ eV is 5.86 Å. The fit yields us an absorption coefficient of 0.000518, which results in the following deposition rate.

$$\text{Deposition rate} = \frac{IMFP}{\text{Attenuation time}} = 5.86\text{Å} \bigg/ \frac{(0.000518 \text{ per second})^{-1}}{60 \text{ seconds/minute}} = 0.182\text{Å/min.}$$

This suggests that the deposition rate is around 10 times lower than with the Auger system, which was not expected. The whole purpose of testing the e-beam evaporator on the Auger system in Aalborg was to understand how to control the deposition rate, such that we could replicate the rate for any setup.

The e-beam evaporator was mounted further from the sample on the XPS system, compared to the Auger system. Under the assumption that the distance was 25 cm in the XPS system and 15 cm in the Auger system, we expect a drop off in the deposition rate of

$$\Delta\text{Rate} = \frac{4\pi 25^2}{4\pi 15^2} = 2.78, \tag{4.1}$$

due to the evaporation beam expanding spherically. But 10 times lower suggest that the e-beam deposition rate is unstable even though the ion current was held at constant 50 nA, when depositing. Although it should be noted that due to the fit being significantly worse than the fit found in section 4.3, the absorption coefficient might be off, and by extension the deposition rate might be inaccurate.

To support the validity of the value for the deposition rate calculated here, we can compare the rate calculated for $E_{exc} = 180$ eV, with the deposition rate at $E_{exc} = 350$ eV. Since these measurements were recorded immediately after each other, on the same sample, we would expect the deposition rate to be the same, even though the excitation energy is different. We repeated the same procedure detailed before, resulting in the fit in figure 4.11.

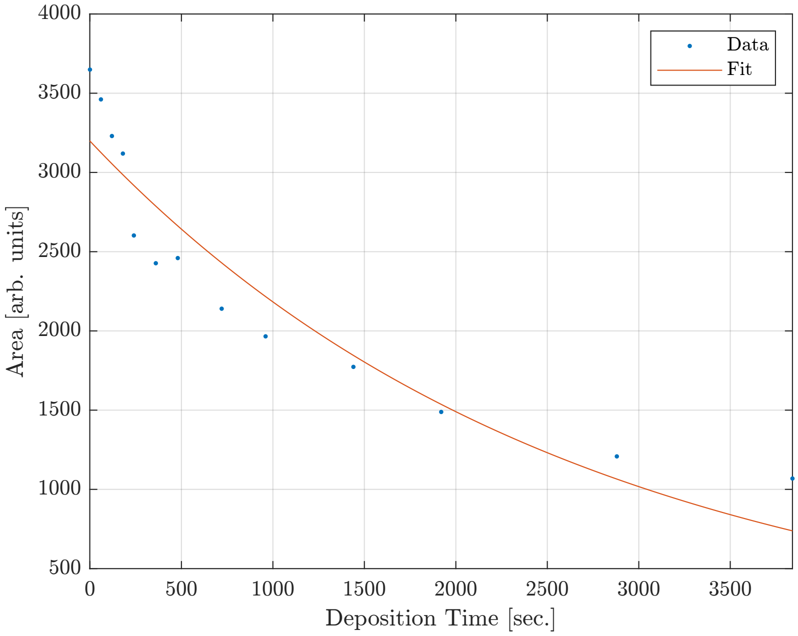

Figure 4.11. Evolution of the Si2p transitions area as boron is being deposited for increasingly longer times. Boron was deposited at room temperature. The XPS scans where made at excitation energy $h\nu = 350$ eV.

It is clear just by observing the figure, that the fit is not good. The fit does not reliably follow the data at any point, showing high deviation for both long and short depositions, which is reflected in the $RMSE = 0.1304$. Obviously, the fit and data still agree that the area of Si2p decreases with deposition time, although the fit being so bad suggests that the data does not adhere very well to the trend prescribed by the Lambert-Beer law.

Since this data was recorded with excitation energy $E_{exc} = 350$ eV, the kinetic energy is $E_k = E_{exc} - E_b = 350 \text{ eV} - 100 \text{ eV} = 250$ eV. For electrons with $E_k = 250$ eV, the IMFP for Si2p is 9.38 Å. Together with the absorption coefficient of 0.000382 yielded from the fit, we calculate the deposition rate to be

$$\text{Deposition rate} = \frac{IMFP}{\text{Attenuation time}} = 9.38\text{Å} \Bigg/ \frac{(0.000382 \text{ per second})^{-1}}{60 \text{ seconds/minute}} = 0.215\text{Å/min.}$$

According to the fit we get a deposition rate of 0.215 Å/min, which is pretty close to the deposition rate calculated for $E_{exc} = 180$ eV, with a percentage deviation of $15,3\%$. Still, it does lend some credibility to the deposition rate being somewhere in this range, as was also determined for the $E_{exc} = 180$ eV scans. Although, the fact that the deviation between data and fit is so large here, compared to the $E_{exc} = 180$ eV measurements, is unexpected since they were recorded after the same depositions. It should also be noted that the decreased deposition rate makes it more sensitive to variations thereby producing depositions that are less likely to accurately follow the Lambert-Beer law.

For the $E_{exc} = 180$ eV measurements, the data follows Lambert-Beer's law well. But at $E_{exc} = 350$ eV, the data indicates that the deposition rate is higher for shorter deposition and lower for longer depositions, see figure 4.11. This is concerning considering we held the ion current constant at 50 nA. To verify the deposition rate calculated here, we will now determine and compare the deposition rate for the second sample as it should ideally be identical to the one calculated for this sample.

4.4.2 Deposition at 450°C

For the second sample which was heated to 450°C while depositing, we determined the deposition rate in the same manner as for the the first sample. For the $E_{exc} = 180$ eV data we got the fit shown in figure 4.12.

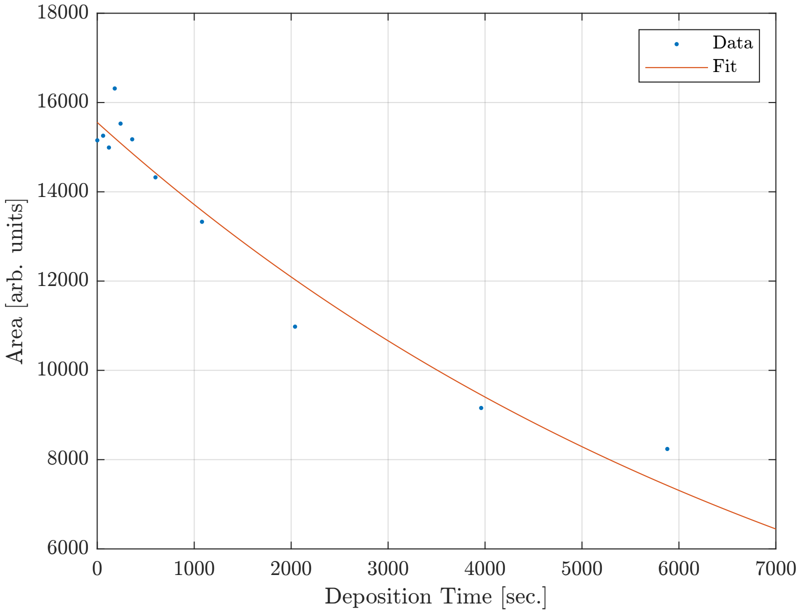

Figure 4.12. Evolution of the Si2p transitions area as boron is being deposited for increasingly longer times. Boron was deposited at 450°C. The XPS scans where made at excitation energy $h\nu = 350$ eV.

The fit is in good agreement with the data, with an $RMSE = 0.0479$, indicating that the fit is of approximately the same quality as the $E_{exc} = 180$ eV fit for the first sample. Much like the 180 eV fit to the data for the first sample, the most notable deviation between fit and data, is for longer depositions. The fit yields an absorption coefficient of 0.000136, resulting in deposition rate

$$\text{Deposition rate} = \frac{IMFP}{\text{Attenuation time}} = 5.86\text{Å} \Bigg/ \frac{(0.0000136 \text{ per second})^{-1}}{60 \text{ seconds/minute}} = 0.0478\text{Å/min.}$$

The deposition rate is close to 1/4 the rate determined for the first sample at $E_{exc} = 180$ eV. We do not suspect this large deviation being due to the quality of the fit, since the $RMSE$, is almost identical to that of the $E_{exc} = 180$ eV fit for the first sample. This large deviation, goes against our assumption, which was that as long as we kept the ion current constant at 50 nA and the distance between the e-beam evaporator and sample remained constant, we would get identical deposition rate between samples. This assumption seems to be too simple, as the deviation is very large, indicating that something else has a significant effect on the deposition rate.

The big factor that has changed between samples is the temperature of the sample when depositing, thus we suspect this might partly be the cause for the deviation. Additionally, since the deposition rate has decreased compared to the first sample, the boron supply in the crucible possibly depleting might be another cause for the significant difference in the rate. Although, we have no way to verify if the amount of boron in the crucible has diminished significantly.

Lastly, we will determine the deposition rate for the $E_{exc} = 350$ eV data of the second sample. Even if the deposition rate is affected by the temperature of the sample or the amount of boron left in the crucible, the deposition rate at $E_{exc} = 180$ eV and $E_{exc} = 350$ eV should be the same since the measurements were taken immediately after each other, at he same temperature.

We fit the $E_{exc} = 350$ eV data in the same manner as previously, resulting in the fit in figure 4.13.

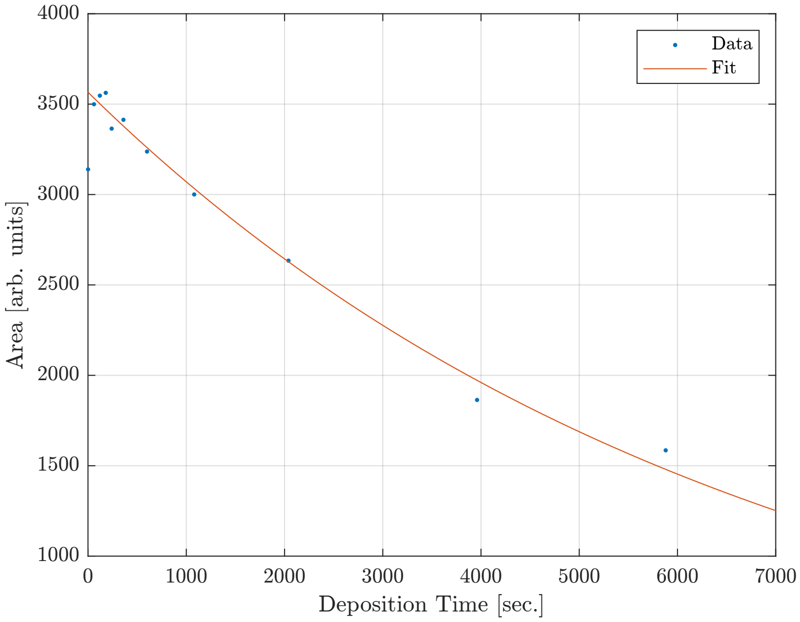

Figure 4.13. Evolution of the Si2p transitions area as boron is being deposited for increasingly longer times. Boron was deposited at 450°C. The XPS scans where made at excitation energy $h\nu = 350$ eV.

This fit shows good correlation to the data, with an $RMSE = 0.0247$. As with the previous fits, the most significant deviation occurs for longer deposition time. The fit gives an absorption coefficient of 0.000146. This results in a deposition rate of

$$\text{Deposition rate} = \frac{IMFP}{\text{Attenuation time}} = 9.38\text{Å} \bigg/ \frac{(0.000146 \text{ per second})^{-1}}{60 \text{ seconds/minute}} = 0.0822\text{Å/min.}$$

The deposition rate at $E_{exc} = 350$ eV, is almost double that of the same sample at $E_{exc} = 180$ eV according to the fit. The difference in deposition rate between samples might be a real phenomena, as we are actually recording data on different samples. But when observing the same sample, the deposition rate is the same, since both the 350 eV and 180 eV data were recorded after the same depositions. Since the difference in deposition rate is not physical it indicates that one of the fits is off due to the quality of the fit, or the way in which the IMFP was determined is not applicable to our sample.

4.5 XPS Measurements of Si(111)$\sqrt{3} \times \sqrt{3}$-B

We carried out XPS measurements at the MATline on the ASTRID2 synchrotron at Aarhus University. High resolution scans of the Si2p, B1s, O1s and C1s peaks as well as valence band spectra were recorded. This procedure was carried out at $T = 25°$C and also at $T \approx 450°$C. Before depositing boron onto the Si(111) surface, we cleaned the sample by annealing, and verified that no oxygen and carbon residue remained by taking high resolution XPS scans of the O1s and C1s transitions. This meant that we now had a clean Si(111) surface.

In this section we will first process the data obtained from the valence band measurements where surface states, Fermi level and doping level will be discussed. Secondly the Si2p peak will be examined by means of characterizing of the surface states, the Si(111) $\sqrt{3} \times \sqrt{3}$-B surface reconstruction and the formation of silicon carbide. Lastly, the oxygen abundance in our spectra will be discussed before the components of the B1s envelope will be decomposed.

4.5.1 Valence band

Measurements of the valence band were made at excitation energies of 41 eV and 180 eV, the former probing closer to the surface and the latter probing deeper into the sample. The measurements were taken over the binding energy range from -1 to 16 eV.

Surface States and Fermi Level

The Si(111) surface is known to have three surface states, S_1, S_2 and S_3, close to the Fermi level[30]. These surface states originate from the Si(111) 7×7 surface reconstruction. By comparing valence band spectra of the clean Si(111) sample with a boron deposited sample, these surface states are easily identified as the differences between these two spectra since the surface states should only appear on the clean Si(111) sample. In figure 4.14 this difference is illustrated and the surface states are indicated by dotted lines.

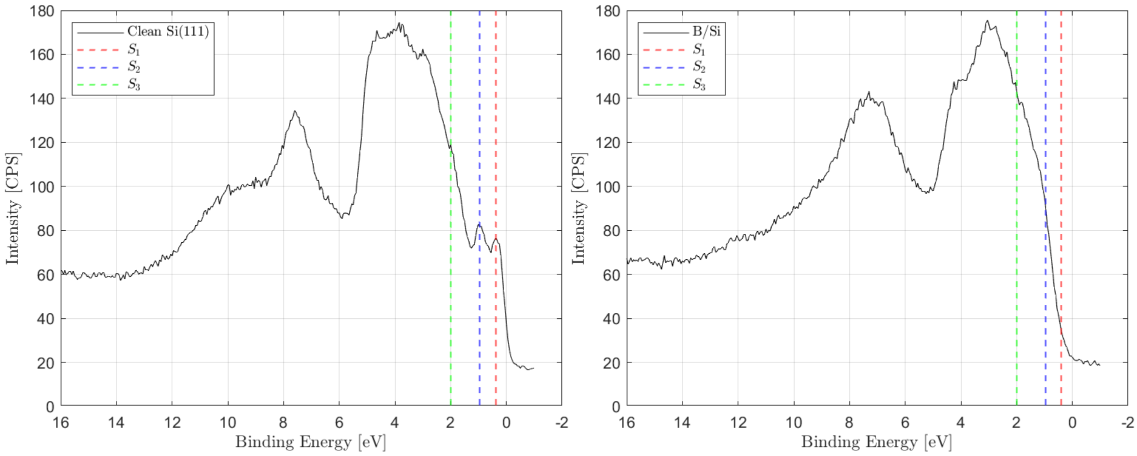

(a) ***(b)***

Figure 4.14. Surface states S_1, S_2 and S_3 located at 0.38, 0.95 and 2.02 eV and indicated by dotted lines on **a** clean Si(111) surface and **(b)** boron deposited Si(111). Excitation energy: 180 eV.

Taking surface state S_1 as a reference S_2 is located at a binding energy of 0.55 eV higher and S_3 is located at a binding energy of 1.60 eV higher than S_1. These relative positions are in good agreement with Uhrberg *et al.*[30].

Next we can determine the Fermi level. For metals the Fermi edge could have been determined by segmenting the spectrum around the first surface state S_1 into a pre-onset, onset and post-onset. Since the peak is approximately a step function, a linear fit could then be made over each segment as can be seen in figure 4.15. The central position between the intersections of the fits determines the Fermi level.

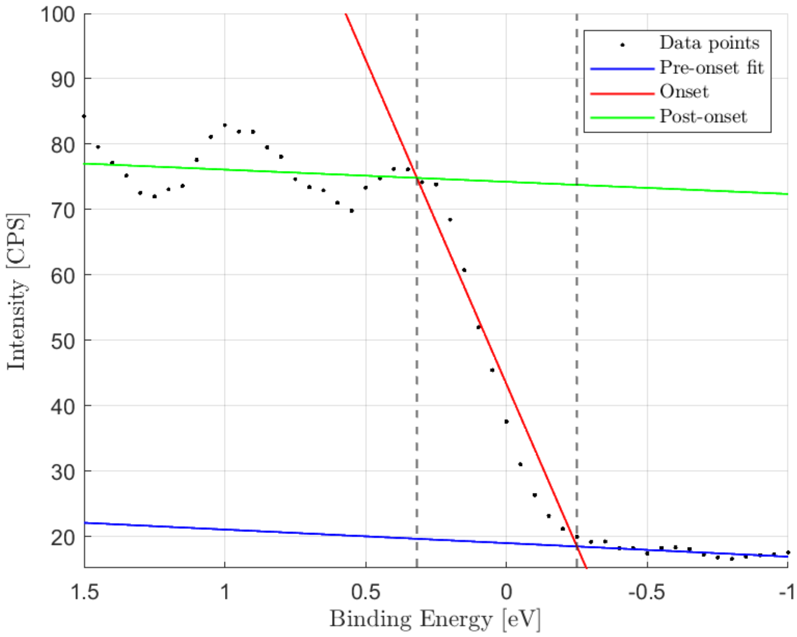

Figure 4.15. Zoom-in on the surface states in figure 4.14 **(a)**. Determination of the Fermi edge if a metal sample was under investigation. The center of the onset between the positions of the intersections of the linear segments would give the Fermi level. Positions of intersections are indicated by dotted lines. Excitation energy: 180 eV.

This is not possible for semiconductors, since the Fermi level is situated in the band gap, contrary to metals. Since our sample is a low doped Si(111) crystal, we can use the fact that silicon is a narrow band gap semiconductor with a band gap of 1.12 eV, and exploit the surface states to determine the Fermi level for this sample. Since we know that the sample is a low doped semiconductor, the Fermi level should be relatively close to the middle of the band gap, meaning that we can not identify the Fermi level with the method utilized for metals.

We observed the S_1, S_2 and S_3 surface states emerging to the low energy side of the valence band, thereby pushing the valence band to lower binding energies. As mentioned, silicon is a narrow band gap semiconductor, so this push is far for the valence band to extend beyond the original Fermi level position, thereby pinning the Fermi level at the edge of the valence band, i.e. the valence band maximum. The push effect of the surface states is visualized in figure 4.16.

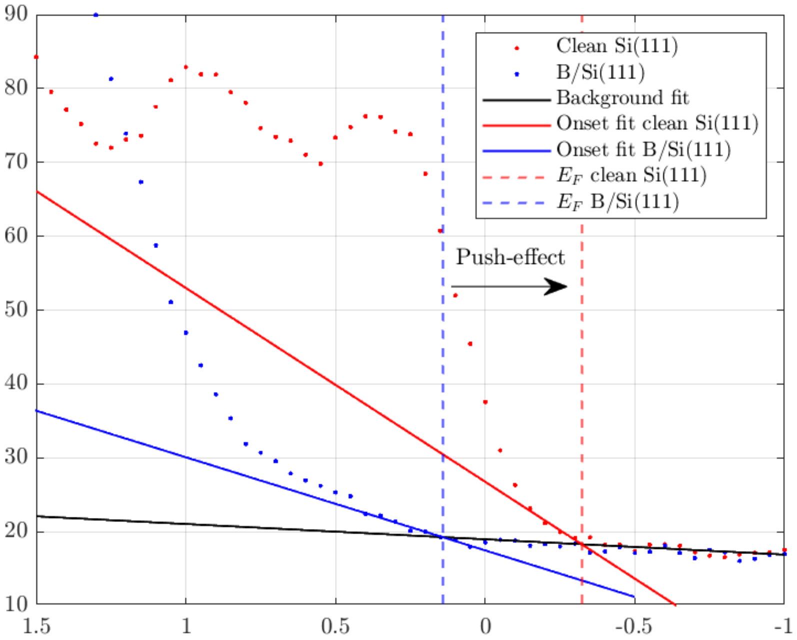

Figure 4.16. Zoom-in on the tails of the valence bands in figure 4.14. The surface of the clean Si(111) surface shifts the Fermi level compared to the Si(111) $\sqrt{3} \times \sqrt{3}$-B surface resembling a push-effect. The push measured as the difference between the Fermi levels is 0.46 eV. Excitation energy: 180 eV.

The Fermi level can now be determined as the position where the valence band coincides with the background signal. This is achieved by using the pre-onset fit mentioned above as background and the low energy end of the S_1 surface state peak as onset. Hence the intersection between these two fits indicates the position of the Fermi level. This procedure of determining the Fermi level is shown in figure 4.17

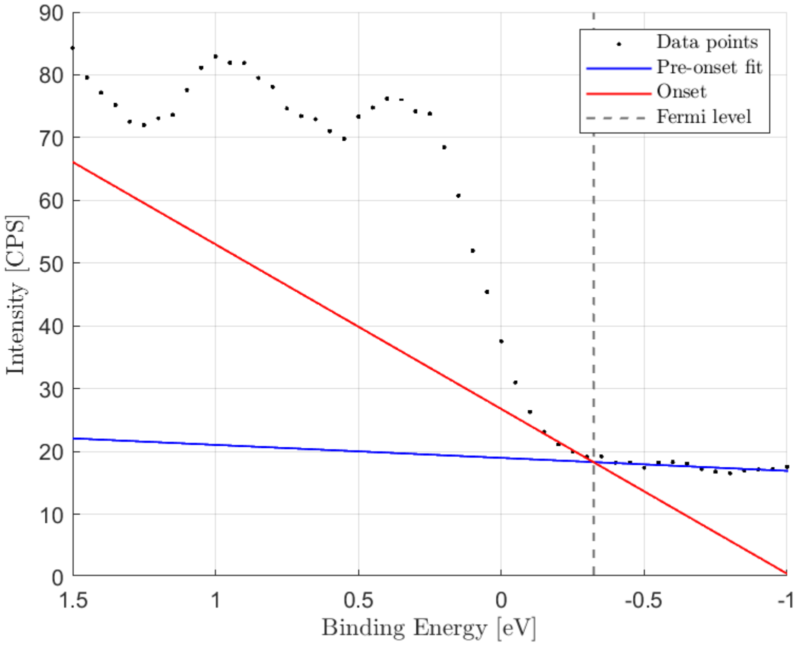

Figure 4.17. Zoom-in on the surface states in figure 4.14 **(a)**. The intersection between the fits of the background and surface states determines the highest occupied state, i.e. the Fermi level, indicated by the dotted line. Excitation energy: 180 eV.

The positions of the surface states can now be calculated with respect to the Fermi edge and are summarized in table 4.1. As mentioned above the relative positions correspond well with experiments performed on an intrinsic Si(111) surface[30]. However the positions of the surface states with reference to the Fermi can not be compared since R. I. G. Uhrberg *et al.*[30] uses other measures to determine the Fermi level. Their method to determine the Fermi level is not described but it is clearly different from ours, since they indicate the Fermi level at a position approximately halfway on the S_1 onset, as can be seen in appendix B. This is the position one would expect if the method for finding the Fermi level of a metal was used and suggests that their positioning of the Fermi level is erroneous.

Peak	Our results	Uhrberg *et al.*[30]
S1	0.72 eV	0.2 eV
S2	1.27 eV	0.8 eV
S3	2.23 eV	1.8 eV

Table 4.1. Comparison of our experimental data with that of the literature[30]. The relative positions between the three surface state are in good agreement. The distances from the peaks to the Fermi level however are shifted due to different methods of determining the Fermi level.

Doping Level

Since we can now determine the Fermi level, the amount of doping in our Si(111) sample is investigated.

Consider the low binding energy end of the valence band in figure 4.14 **(b)**. Using the valence band maximum as a reference we can calculate the position of the intrinsic Fermi level. Comparing this to the actual Fermi level position, determined as the end of the valence band can give us the amount doping of the sample, as described in section 2.6

The valence band maximum is found by making linear fits to the background and the valence band. The intersection of these two lines gives the position of the valence band maximum. The same procedure for finding the Fermi level on the clean sample described above is applied here and the position of the Fermi level is determined to be at -0.75 eV with respect to the valence band maximum. If we assume that the effective masses of holes and electrons are equal, the intrinsic Fermi level is positioned exactly in the middle of the band gap, which is 1.12 eV wide. This means that the intrinsic Fermi level is positioned at -0.56 eV with respect to the valence band maximum. The method of determining the valence band maximum and Fermi level is seen in figure 4.18, where also the intrinsic Fermi level position is indicated.

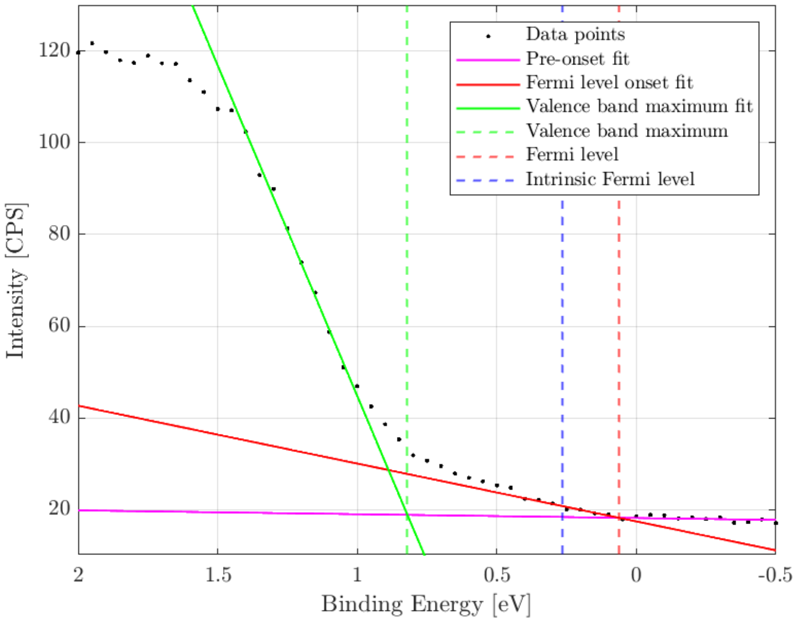

Figure 4.18. Zoom-in on the valence band maximum in figure 4.14 **(b)**. The valence band maximum is determined by finding the intersection between the background and the valence band onset fits. The Fermi level position is indicated as the highest occupied state, i.e. the position where the valence band spectrum first deviates from the background. Positions of valence band maximum, Fermi level and intrinsic Fermi level are indicated by dotted lines.

From figure 4.18 it is obvious that $E_F > E_{Fi}$ if we consider a kinetic energy scale. Hence the sample must be an n-type semiconductor. The electron concentration of the sample can now be determined from equation (2.12)

$$\begin{aligned} n_0 &= n_i \exp\left(\frac{E_F - E_{Fi}}{kT}\right) \\ &= 1.5 \cdot 10^{10}\text{cm}^{-3} \exp\left(-\frac{-0.75\text{eV} - (-0.56\text{eV})}{8.617 \cdot 10^{-5}\text{eV/K} \cdot 300\text{K}}\right) = 2.33 \cdot 10^{13}\text{cm}^{-3}, \end{aligned}$$

where the negative sign in the exponential is added in order to compensate for the inverted energy axis. Since we know that only one type of doping is used for the sample the acceptor atom concentration in equation (2.6.3) is set to zero and isolating the donor atom concentration, N_d, gives

$$N_d = \frac{n_0^2 - n_i^2}{n_0} = \frac{(2.33 \cdot 10^{13})^2 - (1.5 \cdot 10^{10})^2}{2.33 \cdot 10^{13}} = 2.33 \cdot 10^{13} \text{ atoms per cm}^{-3}.$$

This donor concentration corresponds to a very low doped semiconductor as was expected from the information we were given about the sample. Furthermore since the sample is an n-type semiconductor, it is likely doped with phosphorus.

Calibration

Generally, the XPS setup was very stable in regards to eventual shifts of the obtained spectra between measurements, i.e. these shifts were negligible. However while making measurements on the sample where we deposited at 450°C, the beam line had a breakdown resulting in downtime. When the beam line was operating again the spectra had been shifted as can be seen in figure 4.19.

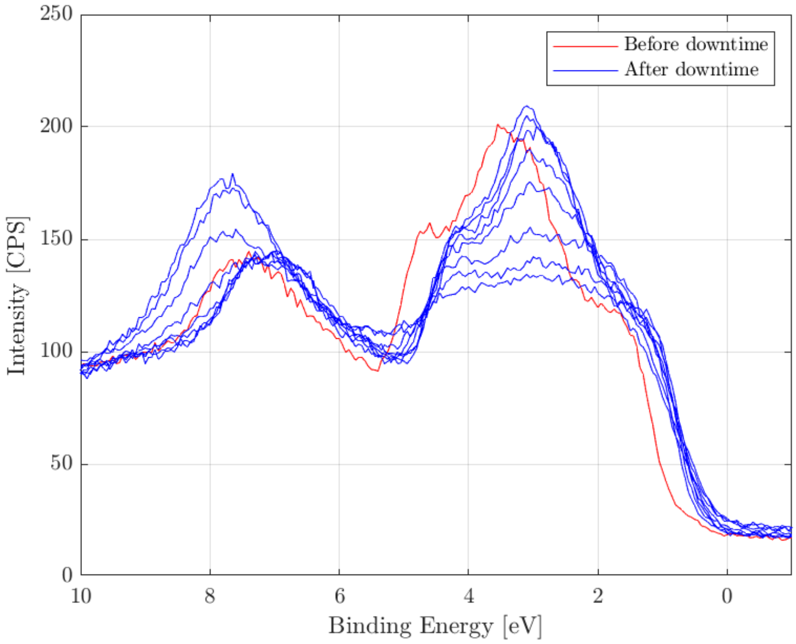

Figure 4.19. The valence band of depositions before and after the downtime are shifted by 0.49 eV. Red line indicates the spectrum before downtime and blues indicate spectra obtained after downtime. Excitation energy: 180 eV.

As mentioned, no oxygen or carbon residue was detected on the sample. This contributed to the quality of the obtained data but it kept us from using adventitious carbon for calibration purposes, as was possible for the sample where deposition was made at room temperature. Instead we used the valence band maximum for calibration in order to cross-reference the spectra from before and after the downtime. For the spectra obtained after the downtime the valence band maximum almost coincided. Finding the valence band maxima in the same manner as earlier in this section enables us to determine the shift and thereby calibrating the spectra. Comparing this valence band maximum to that obtained pre-downtime we find that the spectra are shifted by 0.49 eV. This enables us to calibrate spectra obtained from measurements where no carbon or oxygen residue is present.

4.5.2 Si2p

To further investigate the surface states of the clean Si(111) surface we observed the Si2p peak. We made two high resolution XPS scans of the Si2p peak over the binding energy range from 96 to 108 eV with $E_{exc} = 180$ eV and $E_{exc} = 350$ eV.

Surface States Si2p

At $E_{exc} = 180$ eV, we are probing very close to the surface. Thus, we would ideally be able to resolve the three surface states, which originate from the Si(111) 7×7 surface reconstruction, that we also observed in the valence band spectra of the clean Si(111) surface. We can compare this to the $E_{exc} = 350$ eV spectrum, where we do not expect to

observe the surface states, due to probing deeper into the sample. This leads to a change in the Si2p envelope, as illustrated in figure 4.20. As can be seen, the lineshape of Si2p envelope is clearly different dependent on the excitation energy, which as mentioned before, we suspect is due to the appearance of the Si(111) surface states when we probe closer to the surface. This is especially apparent on the low-energy side of the peak, where the 350 eV profile is broader overall, but there is no obvious shoulder or bump, in contrast to the 180 eV peak where there is a clear shoulder due to one of the surface states.
This is apparent on both sides of the peak. To the low-energy side the 350 eV profile is broader overall and there is a small shoulder at a binding energy of 98.7 eV. At the high-energy side another shoulder is visible for both the 180 eV and 350 eV profiles, though it is more prominent for the 180 eV profile.

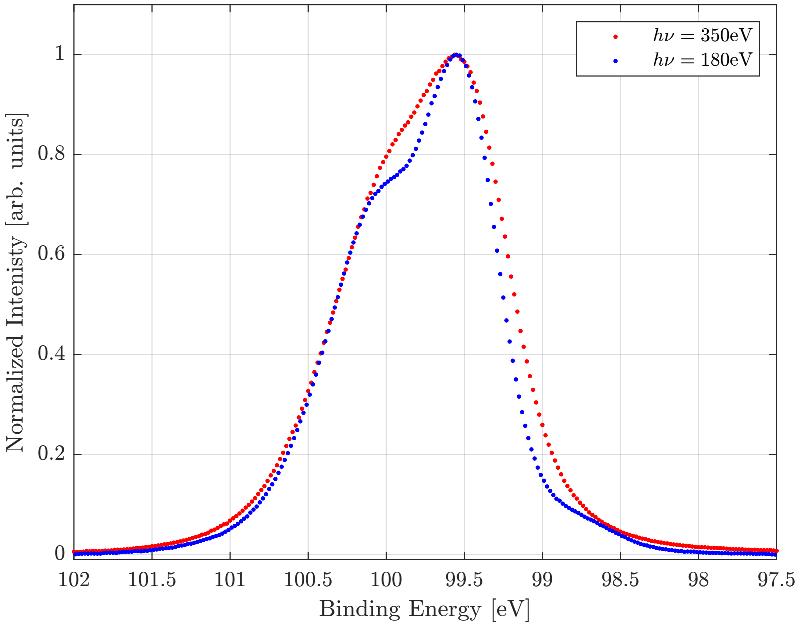

Figure 4.20. Comparison of XPS spectra of the Si2p transition measured at photon energies $h\nu = 180$eV (blue line), and $h\nu = 350$eV (red line).

In section 4.5.1, we discussed silicon valence band spectra, where we identified three surface states in the valence band of the clean Si(111) sample. Since we were able to resolve all three Si(111) 7×7 surface states in the valence band, it is assumed that we would observe the same surface states in the Si2p scans, at $h\nu = 180$ eV. Thus when fitting the XPS data we assume that the Si2p envelope is the combination of bulk Si and the 3 surface states S_1, S_2 and S_3, all of them with 1/2 - 2/3 spin-orbit splitting.

For the fit we used the physical constraints of the 1/2 splitting being half the area of the 2/3 splitting, as well as an energy difference of 0.6 eV. In addition, we assumed that all states had the same FWHM.

Using these constraints we constructed the fit of the Si2p transition at $h\nu = 180$ eV, shown in figure 4.21.

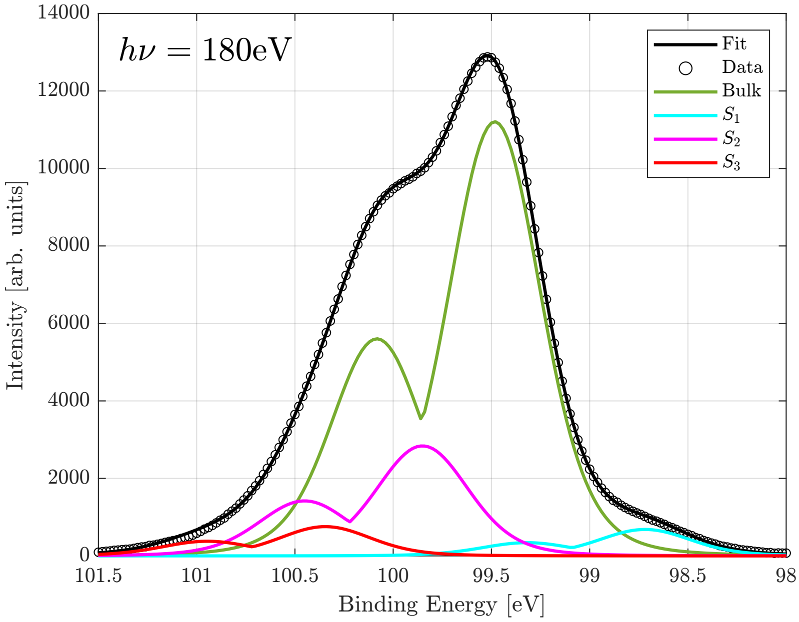

Figure 4.21. XPS spectrum of the Si2p transition at excitation energy $h\nu = 180$ eV, obtained from a clean Si(111) surface at 25°C. The fit consists of bulk Si along with the S_1, S_2 and S_3 surface states. Lineshape: LA(1.92667,2,100).

With a residual STD of only 0.2082, the fit is in very good agreement with the data. It follows the envelope closely at every prominent feature of the Si2p transition. As this fit indicates, we are probing close enough to the surface to resolve the surface states, but bulk Si still dominates. The relevant characteristics and properties of the fit are displayed in table 4.2.

Peak	Rel. Intensity.	BE [eV]
Bulk	1	99.4807
S1	0.0609	−0.76
S2	0.2534	+0.37
S3	0.0674	+0.86

Table 4.2. Relative intensity and binding energy of bulk and surface state peaks for the fit in figure4.21. The binding energy of the $S1$, $S2$ and $S3$ peaks are given relative to the binding energy of bulk Si.

Si(111) $\sqrt{3}\times\sqrt{3}$-B Reconstruction

For the clean Si(111) samples, and throughout depositing boron on the sample at room temperature, the two-peak line shape of the Si2p envelope was conserved. But when depositing B onto the silicon sample at 450°C, there is a very apparent evolution in the shape of the Si2p line-shape, as a new peak appears leading to the new three-peak shape, seen in figure 4.22.

This only occurred for the XPS scans measured at excitation energy $h\nu = 180$ eV, which indicates that this change in line-shape comes from the appearance of surface states due to the Si(111) $\sqrt{3}\times\sqrt{3}$-B reconstruction forming between silicon and boron, as confirmed by LEED in section 4.1. This is supported by the findings of Aldahhak *et al.*[11], who arrived at the same conclusion after performing DFT calculations and making measurements on the B-Si interface. From their DFT calculations they proposed that the Si2p peak consists of a combination of bulk silicon and 5 surface states that occur when silicon reconstructs itself with boron at the interface. To validate this theory, we will investigate if we obtain a fit that is in good agreement with our data, guided by the results obtained by Aldahhak *et al.*[11].

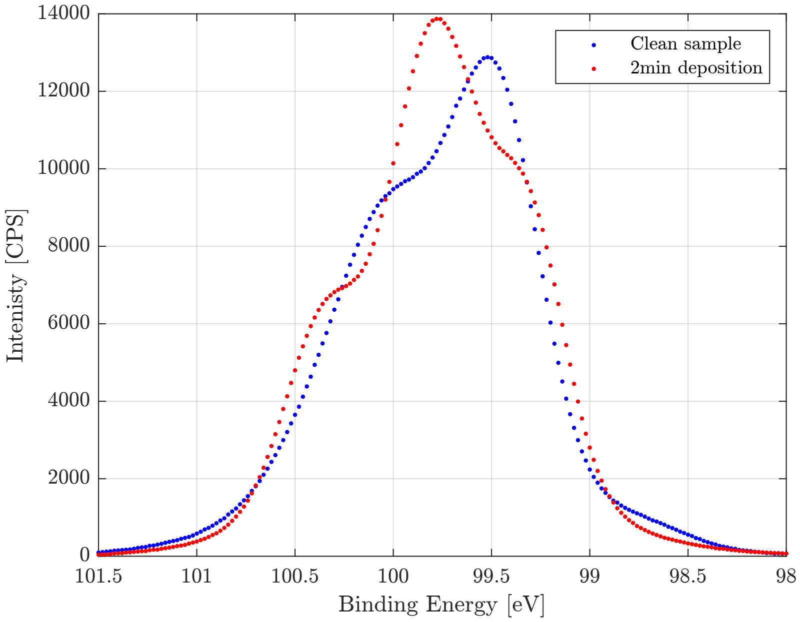

Figure 4.22. Comparison of the XPS Si2p spectrum measured on a clean Si(111) 7 × 7 reconstruction, with the scan after 2 minutes of depositing B at 450°C, where the Si(111) $\sqrt{3}\times\sqrt{3}$-B reconstruction has formed at the B-Si interface. Both scans were measured at excitation energy $h\nu = 180$ eV.

Since bulk Si, and all 5 surface states have a 1/2, 2/3 splitting we actually need to fit 12 peaks to the Si2p envelope. A large number of peaks results in many degrees of freedom. To ensure that the fit is based in reality, we apply some physical constraints. We set the energy splitting to 0.6 eV, and the area of the 1/2 splitting to half the area of the 2/3 splitting for all transitions. We also assume the FWHM is same for all peaks, since they are distinguished by a chemical shift but originate from the same transition. In addition we also constrain the relative intensity of the different surface states according to the DFT calculations made by Aldahhak *et al.*[11], see table 4.3.

Peak	Rel. Intensity[11].	BE (DFT)[11]	BE (exp.)
Bulk	0	0	99.2866
S_1	2/3	+0.01	+0.02
S_2	1/3	+0.10	+0.12
S_3	1/3	+0.41	+0.42
S_4	1	+0.41	+0.43
S_5	2/3	+0.53	+0.52

Table 4.3. Relative intensity and binding energy of the bulk, and surface states constituting the Si2p envelope, as calculated by DFT using the LDA functional, and the binding energy from our fit. The binding energy is given relative to bulk.

For the fit, we let the area of the bulk peak be freely determined by the fitting algorithm, as the DFT calculations made by Aldahhak *et al.*[11] assumed no contribution from the bulk. Finally, having constrained everything except the position of the surface state peaks, we get the resulting fit, displayed in figure 4.23

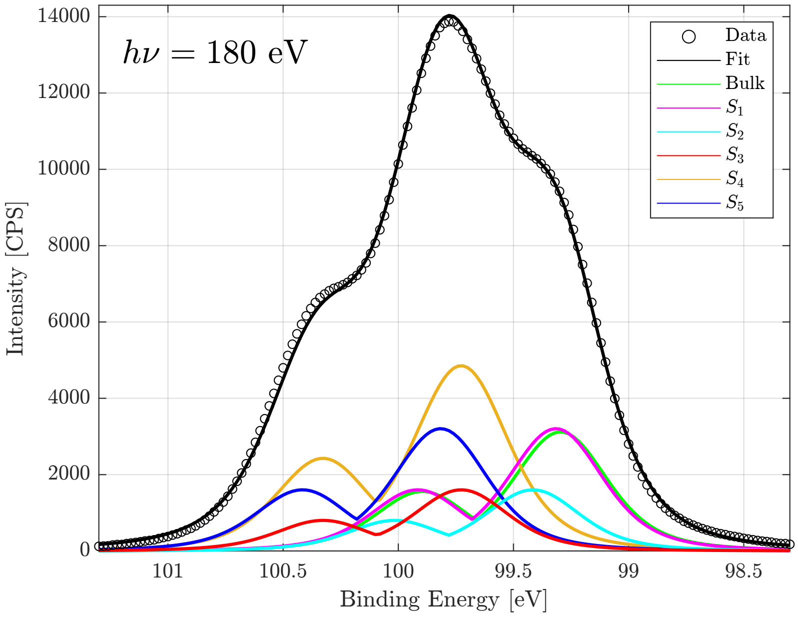

Figure 4.23. XPS spectrum of the Si2p peak obtained at excitation energy $h\nu = 180$ eV after depositing for 2 minutes at 450°C, and the corresponding fit. The fit consists of a convolution of bulk Si and the 5 surface states that occur due the $\sqrt{3}\times\sqrt{3}$-B reconstruction af the B-Si interface. Lineshape: TLA(1.62,0.353,70).

This fit shows good agreement with the data, with a residual STD of 0.7962. While the fit deviates from the data at some points, it quite accurately resembles the general shape of the three-peak Si2p envelope. The positions of the surface states obtained from the fit, are also in good agreement with the DFT calculations reported by Aldahhak *et al.*[11], with a deviation in the binding energy of at most 0.02 eV, as seen in table 4.3.

It should be noted that Aldahhak *et al.*[11] used the PBE-D3BJ and PBE-D2 functional for DFT calculations in addition to LDA. However, as they themselves state, it resulted in virtually identical binding energies, thus we have arbitrarily chosen the LDA functional.

Formation of SiC on Si-B

As previously stated, before depositing boron, we annealed the sample and ensured the sample was clean by verifying that oxygen and carbon were not present in the O1s and C1s high resolution scans.

We continued to take scans of the O1s and C1s peaks between depositions to monitor the oxygen and carbon levels. After the first deposition of 1 min. we observed that carbon had appeared in the C1s scan. The carbon level continued to increase consistently the longer we deposited boron. This occurred for both the sample where we deposited at room temperature and 450°C.

The fact that the carbon abundance grew as we deposited, suggests that the e-beam evaporator is the cause of the appearance of carbon. Even in the best of UHV conditions, a small amount of particles like carbon and oxygen will still be present in the chamber. Thus, a possibility is that as we deposit, some of the remaining carbon atoms bouncing around in the vacuum chambers get caught in the stream of boron atoms and end up on the surface of our sample. For the sample at room temperature, this could be an explanation as in addition to carbon, we also detect an increasing oxygen abundance, the longer we deposit. But for the sample were we deposit at 450°C, we do not observe any oxygen on the sample, only carbon appears and increases with deposition time. It is therefore unlikely that the source of the carbon atoms is the vacuum chamber as we would expect oxygen, which is also present the chambers atmosphere, to end up on the surface.

Instead we suspect that the carbon originates from in or around the e-beam crucible. The e-beam evaporator creates a beam of electrons by heating up a tungsten filament. This electron beam is subsequently used to heat up the crucible, releasing a stream of boron particles. But since the e-beam evaporator had just been exposed to the atmosphere while being transferred from the Auger/LEED system in Aalborg, to the ASTRID2 XPS system in Aarhus, a lot of atmospheric particles end up sticking to the different components of the evaporator.

To remove the particles we degassed the filament and crucible by heating them, but due to not having a mass spectrometer at out disposal, we were unable to monitor the actual amount being degassed. This might have lead to some carbon and oxygen residue remaining on the crucible. Thus, when we then deposited boron onto the sample by heating the crucible, the remaining oxygen and carbon gets degassed as we deposit. This would explain why the oxygen and carbon levels increase with deposition time. This would also explain why only carbon residue remains for the second sample as different elements degas at different rates and temperatures, resulting in oxygen being adequately degassed on the second sample but carbon still remaining.

Carbon also presents itself differently on the two samples. For the sample at room temperature, we see adventitious carbon at $E_b = 284.8$ eV before cleaning the sample. Then when we deposit, we observe carbon again but shifted toward lower binding energy. This behaviour continues, as seen in figure 4.24, the C1s peak shifts with increasing deposition time. The peak shifts from a binding energy close to adventitious carbon, down to a binding energy around $E_b = 283.2$ eV, for the longest deposition. For the second sample, where we heated the wafer to 450°C when depositing, we also saw this energy shift of the C1s peak. Although, contrary to the room temperature sample, the shift was instant instead of gradual. We have adventitious carbon again at $E_b = 284.8$ eV before cleaning the sample. But as soon as we deposit boron the C1s peak shifts to around $E_b = 283.3$ eV, and stays constant with longer depositions.

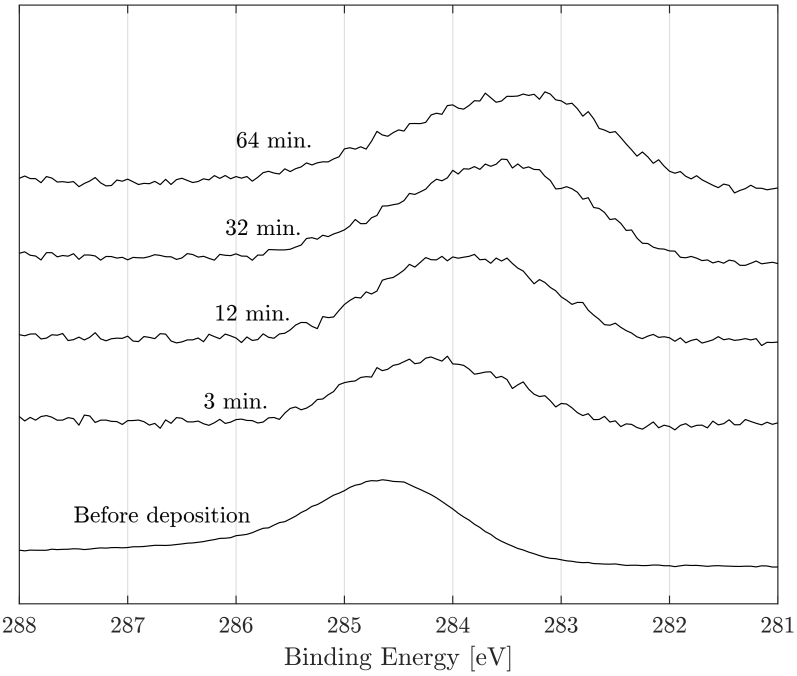

Figure 4.24. Collection of XPS spectra of the C1s transition, made at different deposition lengths at room temperature. All spectra were measured at excitation energy $h\nu = 250$ eV. The spectra are arbitrarily shifted and scaled to demonstrate the evolution in the position.

For both samples we also observe an evolution in the shape of the Si2p peak, especially on the left side of the envelope. As seen in figure 4.25, it appears a shoulder grows on the left side of the Si2p peak, which indicates that some compound is formed as we deposit. Since we do not detect any oxygen on the heated sample, we attribute this shoulder to the growth of a Si-C compound.

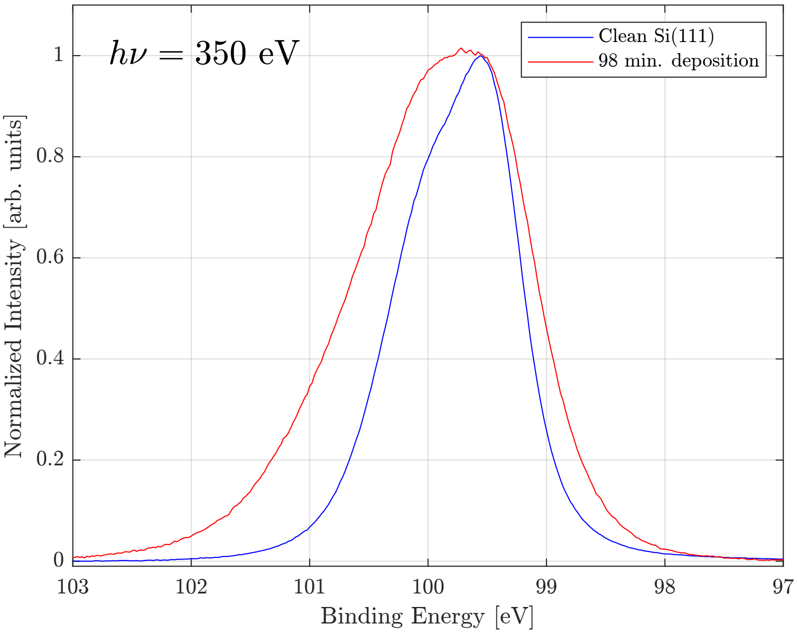

Figure 4.25. XPS spectrum of the Si2p transition measured at photon energy $h\nu = 350$ eV, after depositing boron for 35 minutes.

It is possible that the compound in question is silicon carbide (SiC). This is supported by the shift in the C1s peak for both samples described before, as the formation of SiC reportedly causes a shift of the C1s peak to 283.4 eV according to Delplancke *et al.*[31], which corresponds closely to the shift we observe in both samples. Additionally, Delplancke *et al.*[31] also reports that SiC presents itself at $E_b = 100.40$ eV in the Si2p peak. We investigated if the shoulder seen in figure 4.25, corresponds to this value. This was done by fitting to the $E_{exc} = 350$ eV Si2p scans where we had deposited boron. For the fit we assumed that the Si2p envelope is composed of Si bulk and SiC. We constrain the fit by fixing the spin-orbit splitting of 0.6 eV and the area of the 1/2 splitting to half the area of the 3/2 splitting. Additionally, we assume the line shape and FWHM is identical for the SiC and Si bulk transitions.

The resulting fit, seen in figure 4.26, shows excellent agreement with the data, with a residual STD = 0.1409. The fit follows the data almost perfectly along the whole Si2p envelope. From the fit, we get the position of the SiC component to be $E_b = 100.3$ eV, which corresponds closely to the value reported by Delplancke *et al.*[31]. This means that our proposition that the formation of SiC occurs on our sample is supported both by the C1s and Si2p measurements.

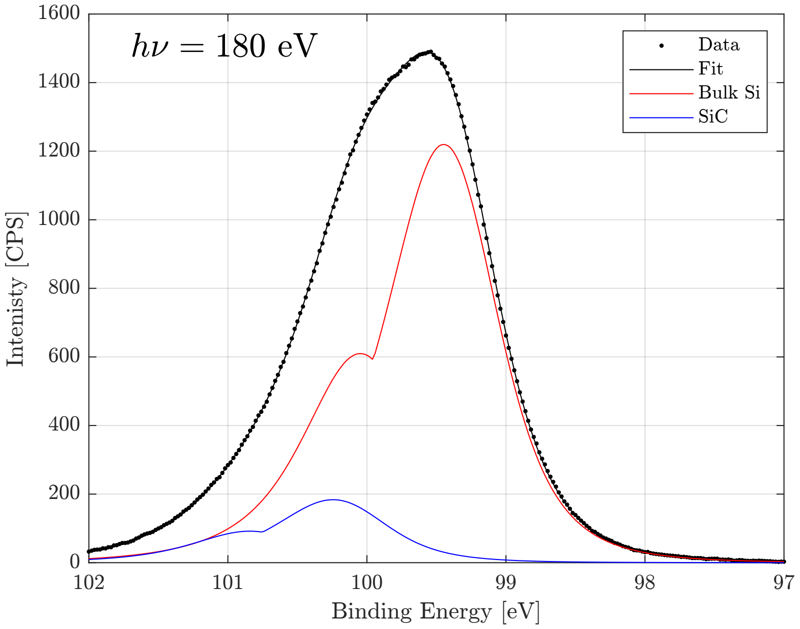

Figure 4.26. XPS spectrum of the Si2p transition measured at photon energy $h\nu = 350$ eV, after depositing boron for 34 minutes. Lineshape: LF(1.33333,1.8,10,54).

Silicon carbide is a compound that requires a lot of energy to form, which might explain why the shift in the C1s peak indicating its formation is gradual for the sample at room temperature. On the other hand it occurs instantly for the sample at 450°C, due to the heat from the sample providing additional energy for the formation, other than the heat from the crucible. It is important to note that SiC is usually only effectively synthesised at temperatures much higher than than what we are dealing with, but there are examples of SiC being synthesized at temperatures closer to our region of interest, as demonstrated by Dasog *et al.*[32], who successfully synthesized SiC at 600°C. Thus, we cannot definitively reject the possibility of the compound formed being SiC, even at a lower temperature than usually observed, without conducting a more thorough investigation, which is outside the scope of this report.

4.5.3 Oxygen Abundance

Measurements of the O1s peak were taken over the binding energy range from 527 to 537 eV at an excitation energy of 610 eV. Despite having UHV conditions in the measurement chamber small amounts of oxygen residue would stick to the sample surface. Since the first three depositions were made in one sequence followed by a downtime of 12 hours after which the last depositions were made we should expect introduction of additional oxygen in the spectra after the break. In figure 4.27, the intensities of the oxygen signal, i.e. the peak area, are plotted for the different deposition times.

As expected there is a small jump in the intensity between 3rd and 4th deposition, indicating that small amounts of oxygen from the vacuum chamber has adsorbed onto the sample during the break. It is impossible to tell how much of the increase in the oxygen signal between 3rd and 4th deposition is due to the adsorption during the break and how much actually comes from the 4th deposition. Fitting the normalized intensities as a function of the deposition time to the following relation , $1 - \mathrm{e}^{-x}$, shows that it is plausible that the oxygen abundance follows the same trend as the boron abundance. Such a correlation is expected until the evaporator is completely degassed since the oxygen should stick to the evaporator, crucible and boron. Furthermore the boron utilized for these experiments was on powder form, enabling oxygen to blend with the boron. This could result in oxygen being deposited along with the boron as the crucible was heated. An RMSE of 0.06304 is obtained for the fit in figure 4.27 which indicates a good correlation with the data.

Downscaling the intensities of the oxygen signal for the depositions after the 4th deposition by a constant also provided us with fits that correspond well with the data. Hence we accept the unmodified measurements for the analysis of the oxygen abundance.

For depositions exceeding approximately 10 minutes, a further increase in the oxygen abundance was observed, as seen in figure 4.27 where data points excluded from the fit are marked as red crosses. These data points clearly do not fit the relation between intensity and deposition time shown by boron. Since we observe this increase for longer deposition times we expect this additional oxygen to stem from parts of the evaporator being heated, resulting in degassing that was not attained for the shorter depositions. This occured again for depositions longer than approximately 20 minutes where large amounts of oxygen seems to be released. This can be realized comparing the very large jump in intensity of the oxygen signal between the last data points in figure 4.27, where the last deposition lasts for 32 minutes.

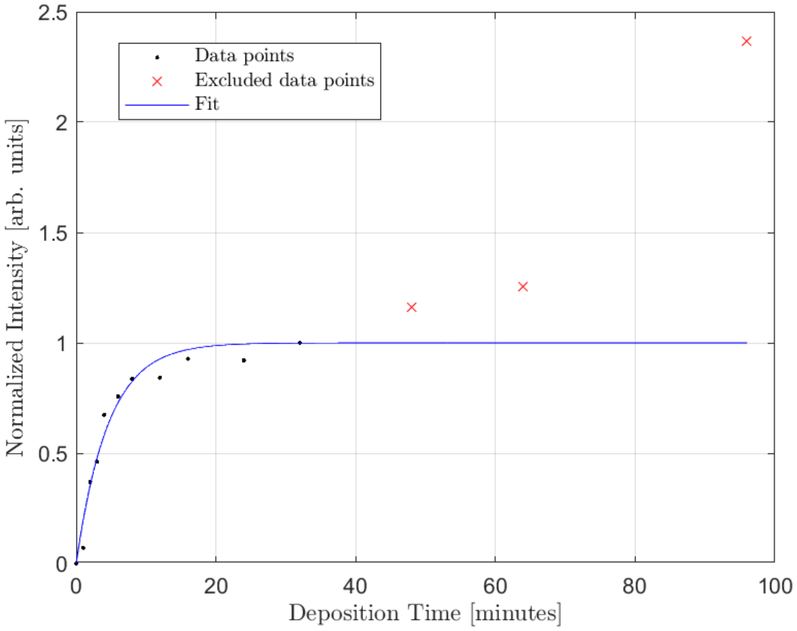

Figure 4.27. Normalized oxygen abundance as a function of deposition time. The oxygen intensity follows the same $1 - \mathrm{e}^{-x}$ trend of the deposition as time as is observed for the boron intensity peaks.

4.5.4 B1s

Spectra of boron were taken at binding energies from 181.5 to 196.5 eV and probed at an excitation energy of 250 eV.

Room temperature

When depositing at room temperature, three obvious components arise when processing the B1s transition; a shift and broadening of the peak and a boron oxide peak to the high energy side, that interferes with the main peak.

Starting with the shift, we can clearly see in figure 4.28 that the B1s peak changes position from 187.53 eV for the first deposition towards higher binding energies as more and more boron is deposited. Then the position reaches a binding energy maximum of 188.36 eV after which it recedes towards lower binding energies and for the last deposition the position of the B1s peak is at a binding energy of 188.25 eV.

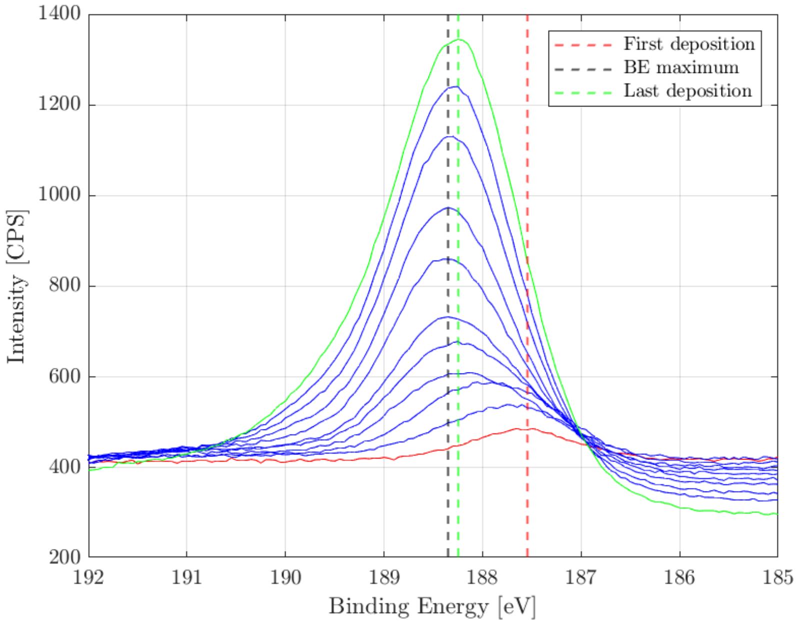

Figure 4.28. The evolution of B1s peak as increasing amounts of boron is deposited. The peak shifts position between 187.53 eV and 188.36 eV. Excitation energy: 250 eV.

Another feature changing as additional depositions were performed is the FWHM. As seen in figure 4.29 the FWHM increases for longer deposition until a local maximum at the 4th deposition (4 minutes). Subsequently the FWHM decreases until a minimum at the 9th deposition (24 minutes) after which the FWHM once again increases.

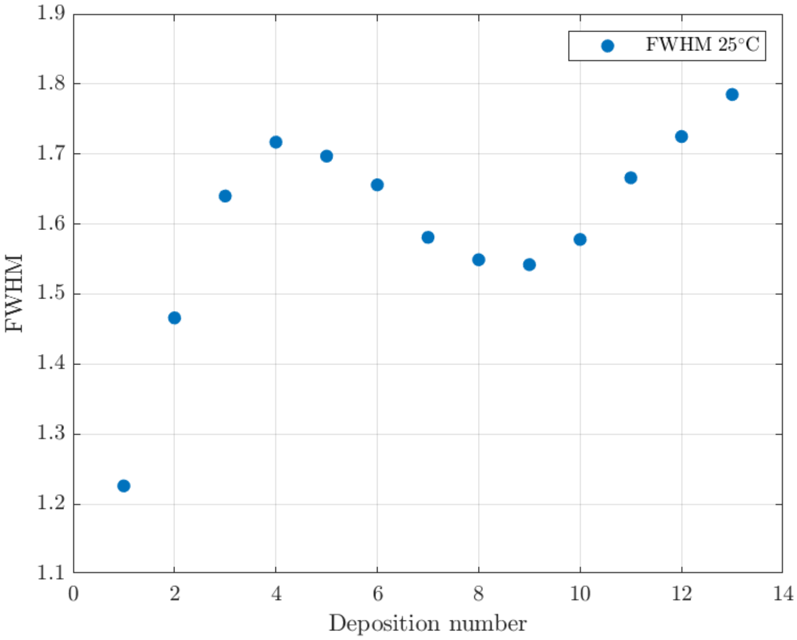

Figure 4.29. FWHM for all depositions at room temperature. The FWHM increases for shorter depositions after which it decreases before an increase is seen at last.

As mentioned earlier in this section, oxygen was present in the spectra of the sample produced at room temperature due to degassing. The amount of deposited oxygen followed the boron abundance except for the last three depositions. This suggest that the increasing broadening could be caused partially by a boron oxide feature positioned at the high binding energy tail of the B1s envelope. In figure 4.30 the B1s envelope of the 5th deposition (6 minutes) is fitted using one peak for elemental boron and one for the boron oxide shoulder. The boron oxide shoulder is located at a binding energy of 191.05 eV, in agreement with Feng *et al.*[33], and the boron peak at 188.2 eV, which is not what would we expect for elemental boron, meaning that the peak is shifted.

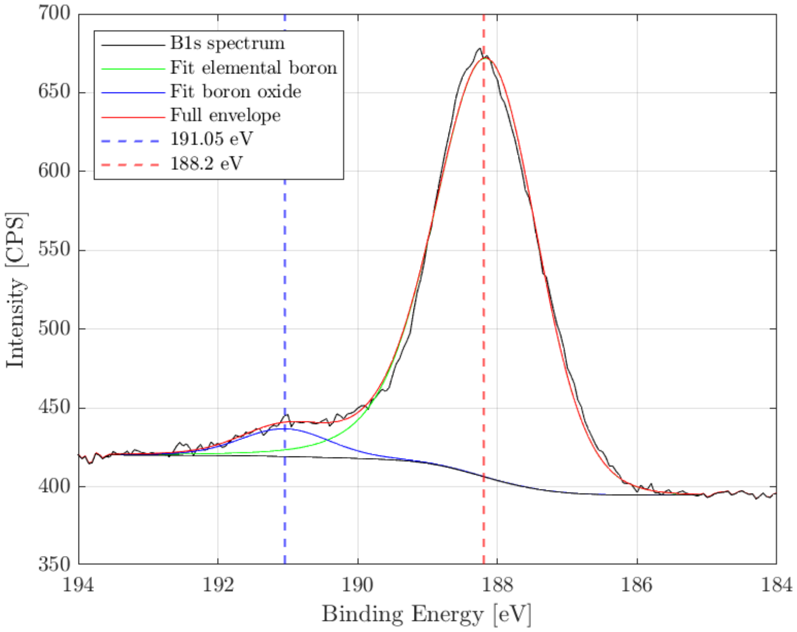

Figure 4.30. Spectrum of the B1s peak, 5th deposition at room temperature. Besides the main peak at 188.2 eV a boron oxide peak emerges at 191.05 eV. Excitation energy: 250 eV. Lineshape: LA(2.1,3.2,87).

With these observations in place we can begin to discuss these results. First the positions of the seemingly 2 peaks in the B1s envelope. The main peak is positioned at 187.53 eV after the first deposition, where only a thin boron layer was present. This value corresponds quite well with the expected value of 187.8 eV for boron[34]. From this position the peak shifts to higher binding energies while the peak broadens as is seen from the increasing FWHM in figure 4.29. We expect that the narrower peaks for shorter deposition to be a result of the boron atoms at the interface being organized in a more ordered manner, than the case is with for the thicker boron layers where we ascribe the broadening to be due to less ordered structures where many chemical shifts may result in many different transitions that ultimately broadens the spectrum. We expect the variations in FWHM after the 4th deposition to be due to random fluctuations, thus the FWHM stabilizes at a rather consistent level subsequently and an amorphous bulk-like layer is then deposited on top.

As we observed carbon in all of our measurements, another reason for the broadening of the main B1s peak could be the formation of a boron carbide peak that interferes with the boron peak. According to Feng *et al.*[33] a boron carbide peak is located at 189 eV. We have not investigated this claim by fitting the B1s main peak to both a boron and a boron carbide peak, but the formation of this compound in the crucible during deposition is likely due to the high temperatures in the crucible. Thus it would not be surprising that this compound appears in our spectra.

Until now the discussion of the broadening of the B1s peak has revolved around the first depositions. As mentioned earlier, the main B1s peak experienced additional broadening at the last depositions, especially for the last three depositions. We expect that this broadening is caused by boron oxide alone. In figure 4.30 the oxide peak is visible to the high binding energy side of the B1s peaks. As we increased the deposition duration, this oxide peak became more and more prominent and appeared less like an individual peak and blended with the main peak, where it added to the asymmetry of the envelope as seen in figure 4.28. This claim is supported by our analysis of the oxygen abundance in section 4.5.3, where we found that large amounts of oxygen were present on the sample following the last three deposition.

The appearance of the oxide peak and of boron carbide could also explain the shift of the B1s peak, since additional peaks at positions close to the B1s peak would cause the envelope to have a maximum at another position.

As a final comment on the B1s peak where we deposited boron at room temperature, the FWHM data could also be interpreted as an increase(until 4th)-decrease(until 9th)-stabilize(at 9th) and then increase due to long depositions (11th ,12th ,13th) where degassing occurred and a lot of oxygen was deposited on the sample, instead of the increase-stabilize model presented above. If this is the case, it indicates that boron is arranged in a structure that is quite ordered for very thin layers right on top of the silicon sample. As more boron is deposited and boron atoms are no longer in direct contact with the silicon sample the increased FWHM indicates less order for the boron not directly affected by the silicon substrate and results in a shift of the envelope. At a certain point the FWHM decreases, indicating a structure that is more ordered than the intermediate layer. As is the case for the former boron carbide and boron oxide model, we once again ascribe the last increase in FWHM to oxides due to the large amounts of oxygen that was deposited at the last three depositions.

Boron B1s peak 450°C

For the first depositions, we observed that the boron peaks were quite sharp and well-defined seemingly unaffected by other peaks. However, as more boron was deposited, resulting in a thicker B-layer, the peaks broadened and adopted a more asymmetric shape. We observed that the lineshape gradually changed as more and more boron was deposited and that the FWHM increased with the thickness of the deposited boron layer. By fitting these B1s spectra we determined the FWHM of the boron peaks to be 0.62 eV after depositing for 1 minute and 1.49 eV after depositing for 130 minutes.

As there is no oxygen present at these depositions, we ascribe this behaviour to the B1s peak actually consisting of two peaks or three peaks. We suspect that the sharp peaks observed for the first depositions are due to the Si(111)$\sqrt{3} \times \sqrt{3}$-B reconstruction since this reconstruction produces very distinct energy levels. Firstly, we ascribe the subsequent broadening, as measurements are made on thicker and thicker boron layers, to another or possibly multiple overlapping peaks, that stem from the additional boron deposited onto the Si(111)$\sqrt{3} \times \sqrt{3}$-B reconstruction which organizes in an amorphous structure, as was also seen at room temperature. This causes an additional peak to arise which could be the source for the broadening and an increased asymmetry of the B1s envelope. Secondly, the broadening could also be caused by the boron carbide peak also discussed for the room temperature sample.

This behavior is visualized in figure 4.31, where the boron peaks of 1 (1st) and 130 (11th) minutes of boron deposition are seen. The spectrum of the peak obtained after 130 minutes of deposition is clearly broadened compared to the spectrum obtained after 1 minute of deposition. In figure 4.31 the broadened spectrum is manually shifted 0.1 eV to lower binding energy to align the peaks for easier comparison.

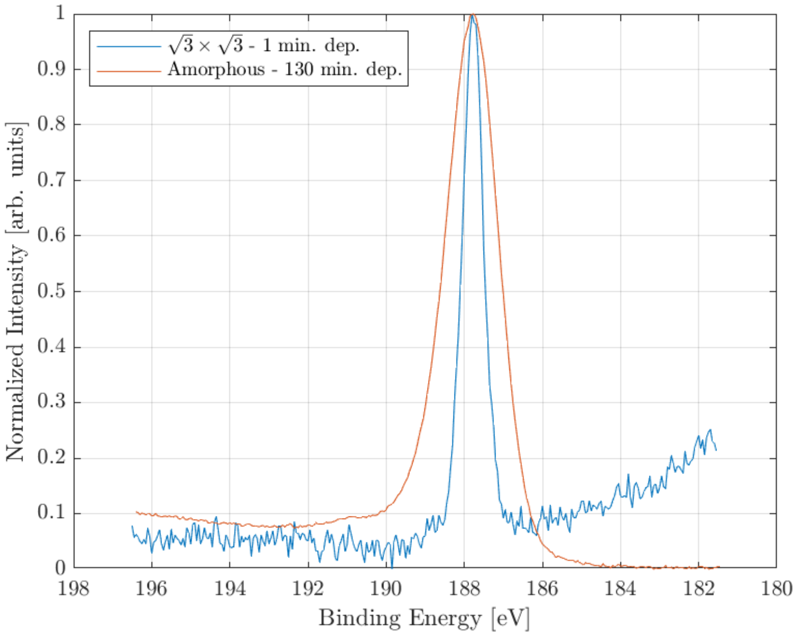

Figure 4.31. Boron spectra obtained after deposition for 1 minute (blue line) presenting a sharp peak indicating the Si(111) $\sqrt{3} \times \sqrt{3}$-B reconstruction. Depositing for 130 minutes (red line) shows a broader peak suggesting that amorphous boron is now present. Peak of 130 minute deposition is shifted manually to align the peaks. Excitation energy: 250 eV.

In the spectra obtained at a sample temperature of 450°C we only observed oxygen at the last three depositions. When comparing the FWHM of the B1s spectra, we observe an almost constant FWHM for the first four depositions followed by a rapid increase and a subsequent stagnation. At last we for the three last depositions the FWHM increases once again exactly when oxygen is present. Therefore oxygen is expected to be the cause of the last broadening in particular, and should be taken into consideration in any analysis where it is present. The evolution in the FWHM is seen in figure 4.32.

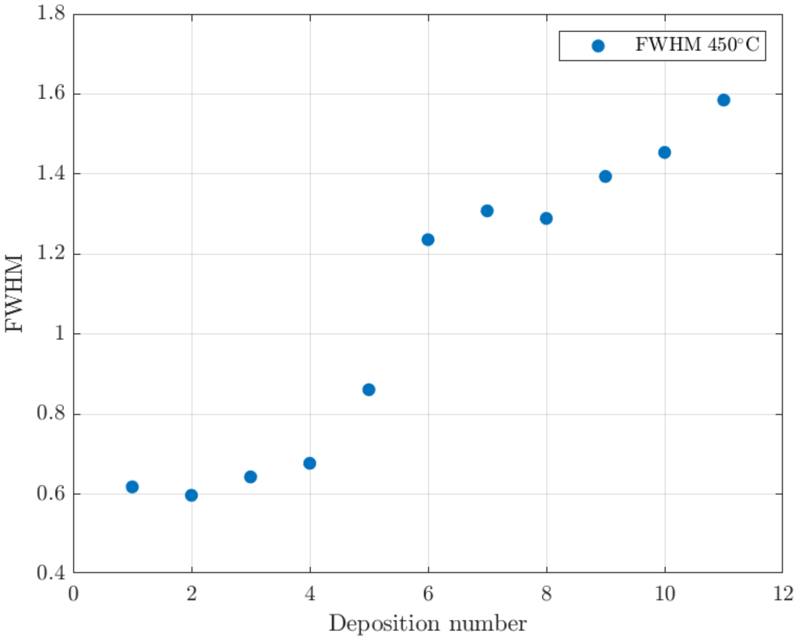

Figure 4.32. FWHM for all depositions at 450°C. The FWHM is stable for the first depositions and increases after the 4th deposition. Subsequently the FWHM stabilizes before one last increase due to large amounts of oxygen being deposited.

Conclusion 5

Boron was successfully deposited on the Si(111) by means of e-beam evaporation at sample temperatures of 25°C and 450 °C. The samples were investigated with LEED, AES and XPS.

The LEED experiments showed that the Si(111)7×7 reconstruction is usually easily obtained by annealing a Si(111) sample at 1000° for 30 seconds. If the sample did not show the Si(111)7×7 within a couple of annealing cycles it was not likely to appear at all, since further annealing would ruin the sample. Depositing small amounts of boron onto the Si(111) sample resulted in LEED patterns of the Si(111)$\sqrt{3} \times \sqrt{3}$-B reconstruction. If deposition of boron on Si(111) had not resulted in the Si(111)$\sqrt{3} \times \sqrt{3}$-B e.g. due to a too large layer thickness, annealing the sample would make the pattern emerge. This confirms that boron is not easily removed from the Si(111) as is the case for oxygen and carbon contaminant that will abandon the surface once annealed. In order to return to a clean substrate after deposition of boron, other techniques as ion sputtering would have to be considered.

XPS measurements of the valence band revealed that three surface states S_1, S_2 and S_3 originating from the Si(111)7×7 reconstruction emerges at the low binding energy side of the valence band, thereby pinning the Fermi level. Thus, the Fermi level position was determined and the positions of the surface states with respect to the Fermi level were found. The relative position between the peaks agreed with findings in the literature, but the position with respect to the Fermi level did not correspond due to different methods of determining the Fermi level. The determination of the Fermi level position, enabled us to calibrate our spectra which was needed due to inconsistencies and it also allowed us to determine the doping level to be $2.33 \cdot 10^{-13}$ donor atoms pr. cm^3, which is a very low amount of doping. Since the Si(111) sample then was an n-type semiconductor, we expect the donor atoms to be phosphorus.

The XPS spectra of the Si2p peak after depositing at room temperature, were compared to the Si2p measurements after deposition at 450°C. Here we examined the difference in the shape of the Si2p peak, indicating that the Si(111) $\sqrt{3} \times \sqrt{3}$-B reconstruction only appeared when the sample was heated to sufficiently high temperatures. This is corroborated by the findings when examining boron deposited Si(111) at room temperature in LEED, where Si(111) $\sqrt{3} \times \sqrt{3}$-B was not observed.

We were able to observe the surface states related to the formation of the Si(111) $\sqrt{3}\times\sqrt{3}$-B reconstruction in XPS, after depositing boron for 2 minutes at 450°C. This Si2p spectrum was decomposed into 5 surface states and bulk, and the resulting fit to the Si2p envelope was in good agreement with the DFT-calculations from the literature.

We also investigated the influence carbon contamination of the S(111) sample had on the Si2p peak, as we deposited. Specifically, the possible formation of Si-C was examined for both the sample heated to 450°C during deposition and the one at room temperature during deposition. A shoulder peak which is in good agreement with the position of Si-C, was identified by decomposing the Si2p into a Si-C and bulk component. This was substantiated by an observed shift in the C1s peak that corresponded to the position of Si-C. Although crystalline Si-C is normally synthesized at higher temperatures, these finding suggest that some type of amorphous Si-C might have formed.

The B1s envelope showed what we interpret as the Si(111)$\sqrt{3} \times \sqrt{3}$-B reconstruction feature, when we deposit at a sample temperature of 450°. It emerges as a narrow peak for the thinnest boron layers and broadens as thicker boron layers are investigated. Simultaneously, the envelope shifts towards higher binding energies. This behavior results from various factors. First of all the narrow peak emerges due to well-defined energy states from the Si(111)$\sqrt{3} \times \sqrt{3}$-B and the thicker boron layers form an amorphous structure. Furthermore contamination of carbon and oxygen also have an obvious effect on the B1s envelope.

Bibliography

[1] NIST, "Standard reference database 71," [Online]. Available: `https://www.nist.gov/srd/nist-standard-reference-database-71`.

[2] C. Davisson and L. H. Germer, "Diffraction of electrons by a crystal of nickel," *Phys. Rev.*, 1927.

[3] L. Meitner, "Über die Entstehung der β-Strahl-Spektren radioaktiver Substanzen," *Zeitschrift fur Physik*, 1922.

[4] P. D. Innes and J. J. Thomson, "On the velocity of the cathode particles emitted by various metals under the influence of röntgen rays, and its bearing on the theory of atomic disintegration," *Proceedings of the Royal Society of London. Series A, Containing Papers of a Mathematical and Physical Character*, 1907.

[5] E. M. McMillan, "The synchrotron—a proposed high energy particle accelerator," *Phys. Rev.*, 1945.

[6] G. Binnig and H. Rohrer, "Scanning tunneling microscopy," *Helvetica Physica Acta*, 1982.

[7] G. Binnig, H. Rohrer, C. Gerber, and E. Weibel, "7×7 reconstruction on si(111) resolved in real space," *Phys. Rev. Lett.*, 1983.

[8] K. Takayanagi, Y. Tanishiro, S. Takahashi, and M. Takahashi, "Structure analysis of si(111)-7×7 reconstructed surface by transmission electron diffraction," *Surface Science*, 1985.

[9] T. M. Grehk, M. Göthelid, U. O. Karlsson, L. S. O. Johansson, S. M. Gray, and K. O. Magnusson, "Clean and cs-exposed si(111)$\sqrt{3} \times \sqrt{3}$:b surface studied with high-resolution photoemission," *Phys. Rev. B*, 1995.

[10] J. E. Rowe, G. K. Wertheim, and D. M. Riffe, "Silicon (2p) surface core-level line shape of Si(111)–B," *Journal of Vacuum Science & Technology A*, 1991.

[11] H. Aldahhak, C. Hogan, S. Lindner, *et al.*, "Electronic structure of the Si(111)$\sqrt{3} \times \sqrt{3}r30^\circ-$B surface from theory and photoemission spectroscopy," *Phys. Rev. B*, 2021.

[12] H. Luth, *Solid Surfaces, Interfaces and Thin Films.* Springer Nature, 2010.

[13] K. Oura, V. Lifshits, A. Saranin, A. Zotov, and M. Katayama, *Surface Science: An Introduction.* Springer Berlin Heidelberg, 2013.

[14] H. Lüth, *Solid Surfaces, Interfaces and Thin Films.* 2010.

[15] H. Bulou, L. Joly, J.-M. Mariot, and F. Scheurer, *Magnetism and Accelerator-Based Light Sources Proceedings of the 7th International School "Synchrotron Radiation and Magnetism", Mittelwihr (France), 2018: Proceedings of the 7th International School "Synchrotron Radiation and Magnetism", Mittelwihr (France), 2018.* 2021.

[16] *Introduction to Optics.* Pearson Education, 2008.

[17] D. Neamen, *Semiconductor Physics and Devices: Basic Principles.* McGraw-Hill, 2012.

[18] R. de Laer Kronig and W. G. Penney, "Quantum mechanics of electrons in crystal lattices," *Proceedings of The Royal Society A: Mathematical, Physical and Engineering Sciences*, 1931.

[19] S. Bengio, H. Ascolani, N. Franco, *et al.*, "Local structure determination of nh2 on si(111)-(7x7)," *Phys. Rev. B*, 2004.

[20] Z. Zhang, S. Hasegawa, and S. Ino, "Reconstruction and growth of ag on the si(111)-sqrt 3 x sqrt 3 -ag surface at low temperature.," *Physical review. B, Condensed matter*, 1995.

[21] M. Katayama, R. S. Williams, M. Kato, E. Nomura, and M. Aono, "Structure analysis of the si(111)$\sqrt{3} \times \sqrt{3}$ r30°-ag surface," *Phys. Rev. Lett.*, 1991.

[22] tectra, *Dual Electron Beam Evaporator: Operating Manual.* 2018.

[23] T. V. Microtech, "Rear view leed with model 8011 electronics operating manual," 2000.

[24] ISA, "Astrid2 – the ultimate synchrotron radiation source," [Online]. Available: `https://www.isa.au.dk/facilities/astrid2/astrid2.asp`.

[25] SPECS, *PHOIBOS 100/150.* 2019.

[26] Y. Makoudi, J. Jeannoutot, F. Palmino, *et al.*, "Supramolecular self-assembly on the b-si(111)-(root 3x root 3) r30 degrees surface: From single molecules to multicomponent networks," *Surface science reports*, 2017.

[27] A. B. McLean, L. J. Terminello, and F. J. Himpsel, "Electronic structure of si(111)-b($\sqrt{3} \times \sqrt{3}$)r30° studied by si 2p and b 1s core-level photoelectron spectroscopy," *Phys. Rev. B*, 1990.

[28] J. D. Levine, S. H. McFarlane, and P. Mark, "Si (111) 7 × 7 surface structure: Calculations of leed intensity and comparison with experiment," *Physical review. B, Solid state*, 1977.

[29] V. Korobtsov, V. Lifshits, and A. Zotov, "Formation of si(111)3 × 3-b and si epitaxy on si(111)3 × 3-b: Leed-aes study," *Surface Science*, 1988.

[30] R. I. G. Uhrberg, G. V. Hansson, J. M. Nicholls, P. E. S. Persson, and S. A. Flodström, "Photoemission study of the surface and bulk electronic structures of si(111)7×7 and si(111)≤3¯×≤3¯:al," *Phys. Rev. B*, 1985.

[31] M. P. Delplancke, J. M. Powers, G. J. Vandentop, M. Salmeron, and G. A. Somorjai, "Preparation and characterization of amorphous SiC:H thin films," *Journal of Vacuum Science & Technology A*, 1991.

[32] M. Dasog, L. F. Smith, T. K. Purkait, and J. G. C. Veinot, "Low temperature synthesis of silicon carbide nanomaterials using a solid-state method," *Chem. Commun.*, 2013.

[33] Y. Feng, R. Qi, L. Jiang, *et al.*, "Chemical modification of b4c films and b4c/pd layers stored in different environments," *Materials*, 2021.

[34] C. Park, G. Shim, N. Balaji, J. Park, and J. Yi, “Correlation between boron–silicon bonding coordination, oxygen complexes and electrical properties for n-type c-si solar cell applications,” *Energies*, 2020.

Appendices

Experimental procedures A

A.1 Cleaning silicon samples

The silicon samples are cleaned by means of electrosometing:

- Set current and voltage to zero.
- Turn on the power supply.
- Set the voltage to the maximum value.
- Turn up the current to 15 A for approximately 30 seconds.
- Turn down the currents over the course of a minute.
- Keep track of the pressure and ensure that UHV ($< 10^{-7}$ mbar) is maintained. For the first cleaning cycle the pressure will reach 10^{-8} mbar.
- Repeat the cleaning procedure one more time or till the sample is properly cleaned.

A.2 LEED/Auger procedure

Electron gun

We turn on the electron gun, by running a current through the filament.

- Turn on power supply.
- Set DPM to ’filament Amps’.
- Turn on filament.
- Increase filament current slowly to 2.2 A, and make sure that the pressure does not change rapidly.

Turn on LEED

- Set mode to ’LEED’
- Turn on high voltage (HV switch).
- Set DPM to ’beam energy kV’.
- Increase energy to 0.1 kV.
- Set DPM to ’emission mAmps’.
- Set ’grid’ to 0.2.
- Set ’mesh mode’ to ’on (local)’
- Set ’mesh voltage local’ close to the electron energy (0.1 kV).
- The LEED pattern can now be adjusted by changing the position of the sample until a symmetric LEED pattern is visible.
- Adjust the mesh energy and beam energy until a clear LEED pattern is visible.
- Change ’focus’ (lens system) and ’A2’ (astigmatism) to obtain a sharper image.
- Different position of the sample yield changes in the LEED pattern.

Turn off LEED

- Turn ’mesh’ all the way down.
- Set DPM to ’emission Amps’.
- Turn ’grid’ all the way down.
- Set DPM to ’beam energy kV’.
- Turn ’energy’ all the way down.
- Turn off high voltage.

Turn on AES

- Set mode to ’Auger’.
- Connect multimeter to read off intensity.
- Turn on ’HV’ (high voltage) switch.
- Increase the energy to 1 kV (Max = 3kV).
- Set DPM to ’emission’.
- Increase ’grid’ to 0.2.
- Set DPM to ’target’.
- Optimize the signal with ’focus’.
- Set DPM to ’emission’.

- Adjust ’grid’ back to 0.2 if it has changed.
- Decrease lock-in amplifier to prevent saturation.
- Find energy maximum by adjusting ’mesh’.
- Set ’phase’ to 90 degrees.
- Adjust the phase until the intensity vanishes.
- To get in-phase signal turn 90 degrees to maximize signal.
- DC-offset: Adjust ’mesh’ to an energy region where no signal is expected.
- Turn ’offset zero’ until signal is zero.
- Set ’mesh mode’ to ’on’ (not local).
- Set lock-in time to 300 ms.
- Energy offset is adjusted in the computer software until the ’start energy’ in the software matches the ’mesh’ energy in the analog system. Beware, the offset may drift between scans.

Turn off AES

- Set ’mesh mode’ to ’on (local)’.
- Turn ’grid’ all the way down.
- Set DPM to ’emission energy kV’.
- Turn the energy all the way down.
- Set DPM to ’filament’.
- Turn the filament current all the way down slowly.
- Turn off ’HV’.
- Turn off filament.
- Set ’mesh mode’ to off.
- Turn off both power supplies.

A.3 Bake-out

Prior to bake-out the UHV chamber is vented. This is done by opening the valve to the ion-pump and shut down the ion-pump, turbomolecular pump and the oil-pump. Subsequently all cables that can not resist the heat of the baking are disconnected. The oil-pump is started and when the pressure decreases in a stable manner the turbomolecular pump is started. The pressure is here approximately $5 \cdot 10^0$ mbar.

Before the bake-out aluminum foil is set to cover all windows for protection and all heating elements are put in the correct places. The UHV assembly is now covered by a heat shield that ensures a constant temperature and the system is baked at 170 °C for 20 hours.

A.4 Degassing filaments

Connect the thermocouple to monitor the temperature inside the vacuum chamber.

Mass Spectrometer

After the heat shield is removed the mass spectrometer is connected. Degassing of the filament for mass spectrometers starts when the mass spectrometer is turned on in the software.

The reason degassing the filament for the mass spectrometer before the other filaments is that the mass spectrometer enables one to monitor the partial pressures of the constituents over time and hence uncover possible leaks that should be sealed. Since hydrogen is an extremely lightweight element it is able to travel both ways through the turbomolecular pump. Therefore the partial pressure of other gasses in vacuum chamber should decrease substantially over time compared to that of hydrogen.

Filament in Electron Gun for Auger/LEED

When the pressure in the vacuum chamber is stable and in the range around $5 \cdot 10^{-8}$ mbar (temperature is here observed to be 70 °C) degassing the filament in the electron gun can be initiated. The filament current is increased in increments of 0.1 A until 2.4 A which is slightly above the operating current of around 2.2-2.3 A. This is done to ensure that further degassing will not occur during operation.

For each increment the pressure will initially increase and after degassing the pressure will again decrease. When the pressure returns to the starting point the another incremental change in the current can be made. The pressure is strictly monitored at each incremental change in the current to make sure that the pressure does not increase uncontrollably.

Sample Holder

A current is sent through the sample and sample holder in increments of 0.1 V to approximately 1.2 V.

Evaporator Filaments

The Dual Electron Beam Evaporator from Tectra used in the Auger and LEED experiments holds two crucibles each with one filament. Both filaments are degassed by setting the current to 2 A at the control panel and subsequently increase the current in steps of 1 A up to 6 or 7 A. At each step the pressure should stabilize and then decrease before moving to the next step. At last the filament current is turned of. While degassing the the evaporator filament the emission current is monitored to control if the emission current is created solely by electrons from the filament or if ionized gas contributes. If the latter is the case then further degassing is needed.

The high voltage is now set to a maximum and the ion trap is turned on. The current for the ion trap is preset to around 2 A.

A.5 Astrid2 Deposition Procedure

- Set manipulator to positions x=8.50 cm, y=13.6 cm, z=24.7 cm $\phi = 335°$ in order to direct the sample directly towards the e-beam evaporator.
- Make sure that the sample is grounded.
- Close gauge between the measurement(aka. preparation) chamber and the beamline (VVS324) and also gauges to the ion pumps (VI1 and VI2). This is not done manually but on the control panel on the computer.
- Open gauge valve between the e-beam evaporator and the measurement valves
- Set the e-beam evaporator to evaporate at an ion current of approximately 50 nA and let it stabilize.
- Remove shield that blocks the sample to initiate deposition.
- When deposition is done return the shield to the original position to block the deposition beam.
- close the gauge valve between the e-beam evaporator and the chamber.
- Shut down the current to the e-beam evaporator filament after deposition.
- Open gauges between beamline and chamber and gauges to the ion pumps.

A.6 Astrid2 Measurement Procedure

- Set manipulator to positions x=8.50 cm, y=13.6 cm, z=10.7 cm $\phi = 170°$ (only z and ϕ are needed to be changed between deposition and measurement.
- Make sure that the the sample is grounded except when measuring the work function where a bias of approximately 9V is applied (a 9V battery is connected) and monitored manually.

Valence Band Comparison B

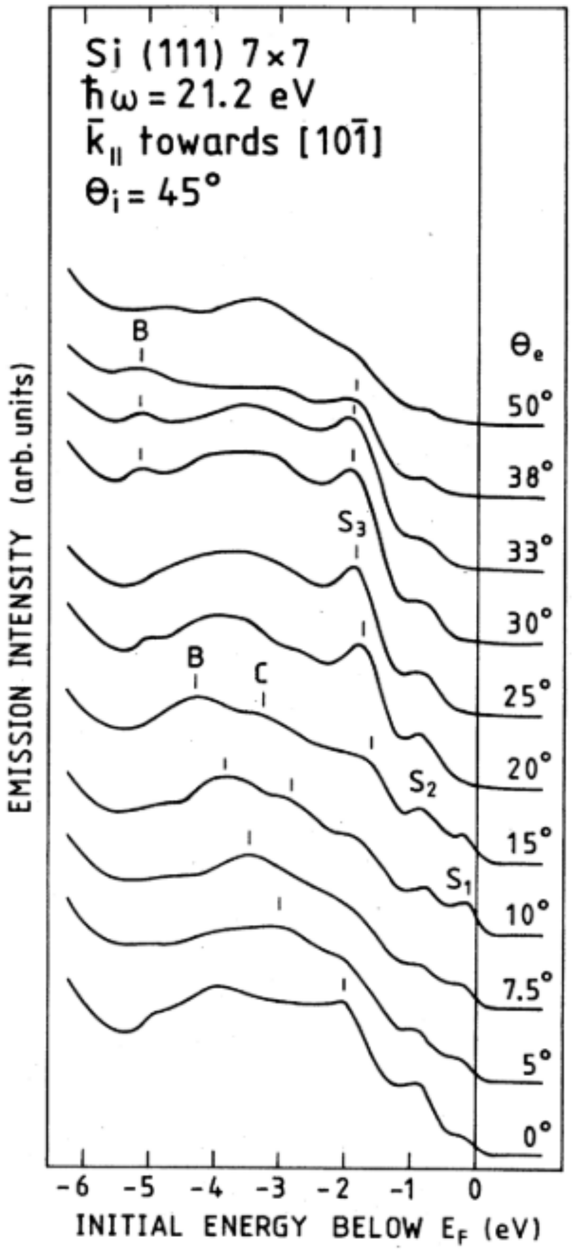

Figure B.1. Valence band measurements showing that the surface states S_1, S_2 and S_3 are pinning the Fermi level. Figure produced by Uhrberg *et al.*[30]